

# Asteroseismology of a Resolved Stellar Binary

By Erica Sawczynek

June 7, 2021

A Senior Honors Project

Presented to the Faculty of the Department of Physics and Astronomy  
at the University of Hawai'i at Mānoa

In partial fulfillment of the requirements  
for the Bachelor of Science with Honors

Committee:

Dr. Jennifer van Saders

Dr. Daniel Huber

Additional Support from Nicholas Saunders, Dr. Jason Curtis  
& Dr. John Tonry.

## Acknowledgements

The biggest of thank-you's to Jen and Dan for their endless support and patience over the past two years of this project. I couldn't have asked for better mentors.

I am grateful to Kurtis for being the best sounding board, always providing honest feedback, and being a consistent voice of reason, to my grandparents for their extra support when I needed it most, to my parents for always being excited about my research, to Kevin for dragging me out of my office to take breaks when I needed it most, and finally to all of my friends—Devin, Suchi & Jessica especially—for their continuous encouragement and enduring endless voice memos.

## Asteroseismology of a Nearby Resolved Stellar Binary

ERICA A. SAWCZYNEC,<sup>1</sup> JENNIFER VAN SADERS,<sup>2</sup> DANIEL HUBER,<sup>2</sup>  
 NICHOLAS SAUNDERS,<sup>2</sup> JASON CURTIS,<sup>3,4</sup> AND JOHN TONRY<sup>2</sup>

<sup>1</sup>*University of Hawai'i at Mānoa 2500 Campus Rd Honolulu, HI 96822, USA*

<sup>2</sup>*Institute for Astronomy, University of Hawai'i, 2680 Woodlawn Dr, Honolulu, HI 96822, USA*

<sup>3</sup>*Department of Astronomy, Columbia University, 550 West 120th Street, New York, NY 10027, USA*

<sup>4</sup>*Department of Astrophysics, American Museum of Natural History, Central Park West, New York, NY, USA*

### ABSTRACT

Gyrochronology is a promising tool to estimate the ages of stars based on their rotation periods. Although well constrained for young stars in open clusters, recent measurements of cool-dwarfs with ages older than 1-2 Gyr have suggested they undergo a period of magnetic braking not included in standard gyrochronology relationships for cool-dwarfs. We study a nearby resolved wide-binary system with a solar-like and an M dwarf component to add a new benchmark to the M dwarf gyrochronology relationship. We generate light curves for both targets utilizing Campaigns 5 & 18 of the K2 Mission. We estimate the age of the solar-like primary via asteroseismology using the light curves from K2 and stellar evolutionary modeling using MESA. Utilizing the K2 light curves and a ground-based ZTF lightcurve, we estimate the rotation period of the M dwarf secondary. We estimate the age of the system to be between  $\sim 3.6 - 4.3$  Gyr and the rotation period of the M dwarf to be  $41.3 \pm 4.1$  days making HIP 43232B one of the first middle-aged M dwarf gyrochronology calibrators.

*Keywords:* Asteroseismology — Gyrochronology — Low-Mass Stars

## Contents

<b>1</b>	<b>Introduction</b>	<b>1</b>
1.1	Stars . . . . .	1
1.1.1	Solar-like Stars . . . . .	2
1.1.2	M dwarf Stars . . . . .	2
1.2	Motivation: The Ages of M dwarfs . . . . .	4
1.3	Gyrochronology . . . . .	5
1.4	Asteroseismology . . . . .	10
1.4.1	Kepler . . . . .	14
<b>2</b>	<b>Purpose</b>	<b>15</b>
<b>3</b>	<b>System Introduction</b>	<b>16</b>
<b>4</b>	<b>Asteroseismology</b>	<b>18</b>
4.1	Lightcurve Extraction . . . . .	18
4.2	Frequency Modeling . . . . .	19
4.3	Stellar Modeling . . . . .	22
4.3.1	Parameter Variations . . . . .	25
<b>5</b>	<b>Stellar Rotation of the Low-Mass Companion</b>	<b>27</b>
5.1	Lightcurve Preparation . . . . .	27
5.2	Rotation Period Measurement . . . . .	29
<b>6</b>	<b>Discussion</b>	<b>30</b>
<b>7</b>	<b>Conclusion</b>	<b>33</b>

**List of Figures**

1	The H-R Diagram . . . . .	3
2	Core-Envelope Decoupling in Rotation . . . . .	8
3	The Surface of the Sun . . . . .	10
4	A Power Spectrum of Solar Oscillations . . . . .	12
5	An Échelle Diagram of the Sun . . . . .	13
6	The HIP 43232 K2 Postage Stamp . . . . .	19
7	The PSD of HIP 43232A . . . . .	20
8	An Annotated PSD and Échelle Diagram for HIP 43232A . . . . .	22
9	MESA Input Physics Variations . . . . .	25
10	Rotation Period Light Curves for HIP 43232B . . . . .	28
11	Rotation and Gaia Color of HIP 43232B . . . . .	31

**List of Tables**

1	HIP 43232: Component Parameter Summary . . . . .	17
2	DIAMONDS NSMC Hyper Parameters . . . . .	21
3	DIAMONDS Fitted Frequencies . . . . .	23
4	DIAMONDS Fitted Amplitudes & Mode Widths . . . . .	23
5	Bellinger (2019) Scaling Relation Input Parameters . . . . .	24
6	MESA Parameter Variation Results . . . . .	26
7	Observed M dwarf Periods . . . . .	29
8	Theoretical M dwarf Periods . . . . .	30

## 1. INTRODUCTION

### 1.1. *Stars*

Stars form in large molecular clouds that are in hydrostatic equilibrium. Hydrostatic equilibrium describes a state wherein the force of gravity acting to compress the cloud and the internal pressure expanding the cloud are balanced. When a cloud is perturbed—either by a nearby supernova or an interaction with another cloud—the hydrostatic equilibrium is disrupted and causes parts of the cloud to become increasingly dense. The gas collapses, the rotation rate of the cloud increases, and a dusty accretion disk forms around the protostar. When the protostar is no longer accreting gas, [Pols \(2011\)](#) considers the star a pre-main sequence star.

Astronomers use a graph called the Hertzsprung-Russell diagram (the H-R diagram) to distinguish both evolutionary state and stellar type. The H-R diagram, seen in [Figure 1](#), shows surface temperature or spectral type on the x-axis and luminosity on the y-axis. There are several luminosity classes ranging from supergiants to main-sequence stars used to describe various stages of a stars life. Main-sequence is a term used to describe one of the most prominent features on the H-R diagram, the diagonal band that runs from the upper left down to the lower right. Main-sequence stars actively fuse hydrogen into helium in their cores. A pre-main-sequence star is a star that is currently moving on to the main sequence, but has not started hydrogen burning in the core yet.

Many stars are in orbits with another star—a binary—or multiple stars, suggesting stars often form with a companion ([Abt 1983](#); [Duquennoy & Mayor 1991](#)). [Whitworth et al. \(1995\)](#) proposes two main methods of multi-star system formation. In the first method, the accretion disk around the protostar spins up quickly, becomes unstable, and divides into two protostellar disks ([Chapman et al. 1992](#); [Whitworth et al. 1995](#)). In the second method, the accretion disk spins up slowly, forming spiral arms; the arms then detach and form other stars ([Whitworth et al. 1995](#)). Stars born in the same cloud

that form at the same time are known as coeval (Pols 2011). Coeval stars are powerful tools for testing stellar evolutionary models. In this work, we use the age of one star in a binary system to infer the age of the companion star.

#### 1.1.1. *Solar-like Stars*

A solar-like star describes a star that has properties similar to our own Sun in terms of metal abundance, mass, radius, spectral type, temperature, or general behavior. A one solar-mass Sun-like star moves slightly up and left on main-sequence (moving towards the upper left of the linear trend in Figure 1) over about 10 billion years as it burns hydrogen in its core. When the solar-like star has fused all of the core hydrogen into helium, the outer layers of the star expand. As the stellar envelope expands, the outer surface of the star cools, the hydrogen burning shell begins to form, and the star moves to the right on the H-R diagram, becoming a subgiant star. Finally, as the hydrogen shell burns, the radius and luminosity of the star continue to increase as the star evolves on the red giant branch.

Our Sun is a G2V star, where G2 indicates the surface temperature (around 5,800 K), and V indicates the luminosity class main-sequence. We are at a distinct advantage when it comes to studying stars similar to our Sun because we can study our Sun in greater detail than other stars. As a result, solar-like stars have very well-calibrated evolutionary models.

#### 1.1.2. *M dwarf Stars*

M dwarf stars are a subset of main-sequence stars, located at the bottom right side of the H-R diagram, commonly known as red dwarf stars. Over 80% of the stellar population is comprised of M dwarf stars, making them the most numerous stars in the galaxy (Engle & Guinan 2011). M dwarf stars are especially interesting due to their extremely long lifetimes, which are upward of 11 trillion years (Adams & Laughlin 1997). These long lifetimes make M dwarfs rare laboratories to study planetary

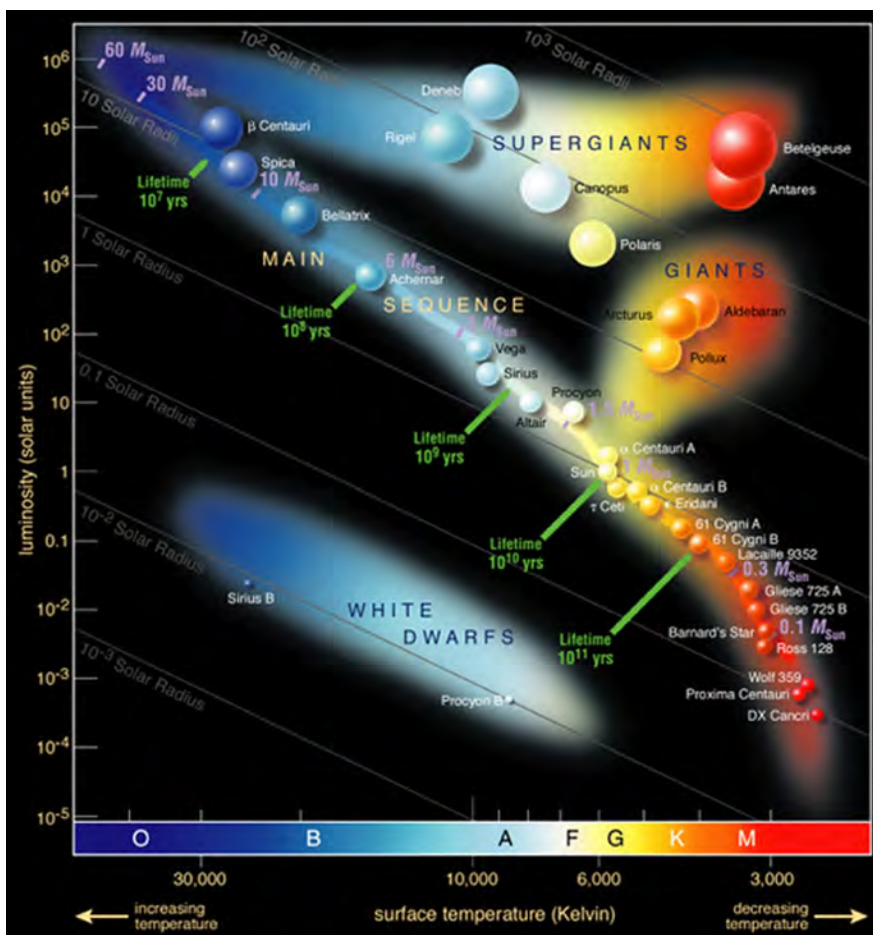


**Figure 1.** The Hertzsprung-Russell (H-R) Diagram plots the spectral type of star vs. its absolute luminosity, which can help to show where a star is in its evolution.

evolution (Shields et al. 2016). The lifetimes of low mass stars are so long because they use less energy to support against gravitational collapse, conserving fuel (Adams & Laughlin 1997; Engle & Guinan 2011).

M dwarfs are objects of interest due to the long lifetimes detailed above, as well as their close habitable zones (Engle & Guinan 2011). Hart (1979) and Kasting et al. (1993) define the habitable zone as the region around a star where a planet with an Earth-like atmosphere can maintain liquid water on its surface. It is no coincidence that small, rocky, Earth-mass planets are often found around M dwarf stars because the occurrence of small planets is higher among low mass stars (Dressing & Charbonneau 2013). Also, planets orbiting around M dwarf stars are easier to discover using common

planet-finding techniques (Shields et al. 2016). One common method of detecting planets is through observations of planetary transits. A transit describes the time when a body passes directly between a larger body and an observer; in this case, when a planet crosses between a telescope and the front of its host star. M dwarf stars are relatively low luminosity meaning that the orbits of planets in the habitable zones of M dwarfs is closer to the star, implying that these planets have shorter orbital periods, increasing the likelihood of observing a transit because there are more frequent planetary transits (Goulding et al. 2012; Nutzman & Charbonneau 2008; Shields et al. 2016). A combination of these two traits makes the planets around M dwarfs the easiest places to look for biological evolution and, in turn, life (Shields et al. 2016).

However, the magnetic activity in M dwarfs can cause large stellar flares (Hawley & Pettersen 1991; Lammer et al. 2013). M dwarf flares produce extreme ultraviolet radiation, which can negatively affect the atmospheres of the surrounding planets (Lammer et al. 2007). Flares from M dwarfs are larger and more frequent when the star is young, with M dwarfs from 0.5-1 billion years (Gyr) showing high saturation levels of flares (Lammer et al. 2009). After 1 Gyr of constant bombardment, the planets around the M dwarf star could have greatly thinned atmospheres, which can result in a drastic loss of any surface water and surface life (Engle & Guinan 2011; Luger & Barnes 2015; Shields et al. 2016).

Determining the age of an M dwarf star is typically the only way to estimate an age of the planetary system around the M dwarf. Knowing the age of these systems allows the stability and dynamic evolution of the system to be evaluated (Engle & Guinan 2011). All are of the above are necessary ingredients in discussing the habitability of planets around M dwarfs.

### 1.2. *Motivation: The Ages of M dwarfs*

Despite the obvious advantages of targeting M dwarfs for planet surveys, M dwarf stars are notoriously difficult to characterize. In particular, while stellar ages are

key ingredients for a complete picture of exoplanet evolution and demographics, most age-dating techniques fail when applied to M dwarfs (Soderblom 2010). Traditional isochrone fitting techniques, using an H-R diagram position, are well-suited for stars of solar mass or greater on the main sequence, but fail for M dwarfs which only move perceptibly on the main sequence over timescales much longer than the age of the Milky Way (Barnes 2007). Similarly, while asteroseismology—gathering information about stars through their observed oscillations—can provide precise ages on the main sequence (e.g. Creevey et al. 2017; Silva Aguirre et al. 2017), detecting solar-like oscillations in stars with masses lower than  $\sim 0.8M_{\odot}$  is infeasible with the sensitivities of current observational facilities (Rodríguez et al. 2016; Chaplin et al. 2011).

Metallicity-age relations, or using the correlation between stellar compositions and ages, are poorly understood relationships and generally subject to wide scatter. The lithium depletion boundary, or using a measure of surface Li abundance to infer age, can only be used for stars within a certain mass and temperature range, making it impossible to estimate the age of low-mass field M dwarfs. Activity-age relationships, or using the magnetic activity of a star to estimate the age of a star, are difficult to use because little is known about M dwarf activity cycles. Finally, kinematics—tracing the motion of a group of stars back to when they formed or mapping the velocity dispersion of a group of stars—may have a promising future as an age-dating technique (see Angus et al. 2020; Lu et al. 2021), but is currently unable to constrain the age of an M dwarf better than a few billion years (Soderblom 2010).

### 1.3. *Gyrochronology*

Gyrochronology, first coined by Barnes (2003), or using a stars' rotation period to estimate its age, shows promise in being able to estimate the ages of M dwarfs. Rotation of stars is often measured using spot modulation or by watching as a star spot moves in and out of view as the star rotates. By taking precise measurements of the star's brightness over an extended period of time, we can track how long it takes for the star

to undergo one rotation giving us a rotation period. An image of an example of a star spot on the Sun can be seen in Figure 3.

Skumanich (1972) first claimed that for solar-like stars, rotation rate, lithium abundance, and chromospheric magnetic activity all decrease at a rate proportional to the square root of the age. We know stars are born on to the main sequence spinning rapidly, and they lose angular momentum, or spin down, as they age (Parker 1958; Kraft 1967; Skumanich 1972; Soderblom 1983). The convection and differential rotation in stars fosters turbulence and the magnetic dynamo in the star (Aerts et al. 2019). The subsequent mass loss and magnetic field lead to angular momentum loss of the stellar envelope resulting in rotational spin-down (Weber & Davis 1967). Barnes (2003) noted a wide dispersion of rotation rates among open clusters but suggested there are three primary rotational sequences: slow and ultra-fast rotators of low mass that spin down with time, and more massive fast rotators that hardly spin down at all. Kraft (1967) identified a break on a graph of spectral type versus surface gravity between the ultra-fast and slow rotators, now called the Kraft break. On one side of the break there are more massive stars with negligible convection zones and on the other side there are stars with thick convection zones. The slow rotator sequence is comprised of stars redder than the Kraft break that slowly lose angular momentum over time. The fast rotators, or the “radiative sequence”, are comprised of stars bluer than the Kraft break, but due to a lack of surface convection that drives a strong magnetic field, do not spin down over time. Finally, the cool, ultra-fast rotator sequence has no dependence on color, but branches off of the slow rotator sequence and also spins down over time. Barnes (2003) also finds that the ultra-fast rotating stars move on to the slow rotator sequence over time.

Several subsequent studies (e.g Barnes 2007; Mamajek & Hillenbrand 2008; Meibom et al. 2009, 2011) have continued to calibrate gyrochronology mass-rotation-age relationships using open clusters, finding gyrochronology can estimate the ages of solar-type

stars within 10% (Meibom et al. 2015). However, as Epstein & Pinsonneault (2014) note, although there is wide success with estimating ages using empirical gyrochronology relationships, there are still limitations in our understanding of how spin down occurs in stars. Much of the complexity comes from a lack of understanding of angular momentum transport within stars and angular momentum losses from the stellar wind. Star-forming regions set constraints on initial angular momentum rates, and observations from open clusters provide angular momentum benchmarks for specific ages, but calibrators become increasingly difficult to find at older ages (Epstein & Pinsonneault 2014). More recently Gruner & Barnes (2020); Curtis et al. (2020); Agüeros et al. (2018); Delorme et al. (2011) and Douglas et al. (2016) have explored extending gyrochronology relationships into the cool-dwarf regime using older clusters of coeval stars as benchmarks. However, while the ages of M dwarfs are easiest to estimate precisely in open clusters, most nearby open clusters are young ( $\sim < 1$  Gyr), which limits the age of the calibration sample for M dwarf gyrochronology (Agüeros et al. 2018; Curtis et al. 2019, 2020; Gruner & Barnes 2020; Delorme et al. 2011; Douglas et al. 2016). As a result, current gyrochronology relationships—extrapolated from trends using more massive stars—fail to reproduce newly available cluster data for low-mass stars (see Curtis et al. 2020).

The simplest angular momentum loss model comes from Kawaler (1988), which starts with an initial distribution of protostar rotation rates and evolves to reproduce the Skumanich (1972) relationship. Pinsonneault et al. (1990) later showed this relationship did not produce results consistent with open cluster data and suggested three additional refinements: star-disk interactions (changing initial rotation periods), mass-dependent saturation thresholds (changing the spin down in rapid rotators), and core-envelope decoupling (changing the internal redistribution of angular momentum). As relevant to the scope of this thesis, we will only focus on how including core-envelope decoupling in stellar rotation models may improve gyrochronology results for low mass stars.

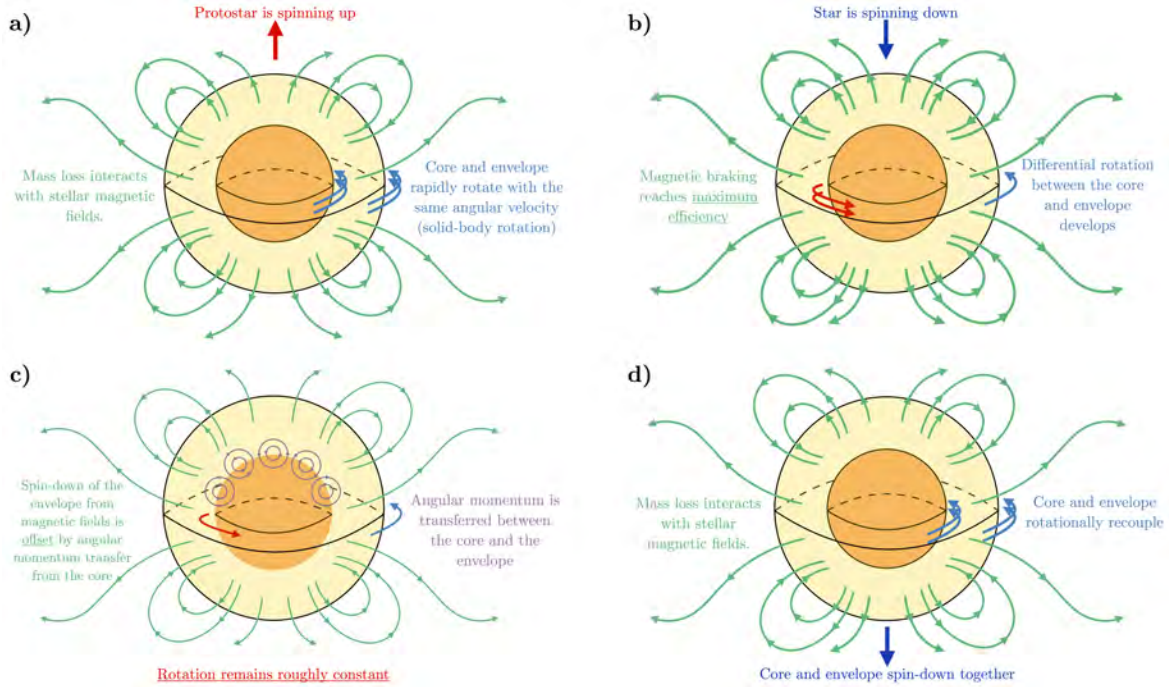


**Figure 2.** Core-Envelope rotation broken down into 4 main steps. *Panel a:* Star spins up as a solid-body. *Panel b:* Differential rotation and stellar spin-down starts. *Panel c:* Angular momentum transport offsets magnetic wind, envelope remains constant. *Panel d:* Core and envelope re-couple, rotational spin-down resumes.

Internal angular momentum transport is often modeled using a “two-zone” model such as in Spada & Lanzafame (2020). Similarly to Lanzafame & Spada (2015), Spada & Lanzafame (2020) assumes a two-zone model comprised of a radiative core and a convective envelope that each rotate with a respective angular velocity (MacGregor & Brenner 1991). The two-zone model for gyrochronology, allows for differential rotation with radius. The Spada & Lanzafame (2020) model is especially interesting for low-mass stars because it introduces a period of rotational evolution where spin-down is effectively stalled. Panel a in Figure 2 shows a pre-main-sequence star rapidly rotating as a solid body. In Panel b the star spins up, magnetic braking reaches maximum efficiency, and differential rotation develops as the envelope of the star begins to spin down. As the angular momentum loss rate slows with the decreasing rotation rate, the angular momentum that is transferred between the core and the envelope offsets

the angular momentum loss of the envelope from the magnetic field. There can be a phase, depicted in Panel c, when the rotation of the envelope remains roughly constant. After some time, the core and envelope re-couple bringing the star back to a rigid body rotation (Panel d). Other critical assumptions from [Spada & Lanzafame \(2020\)](#) that affect spin-down are:

1. Initially all stars are rigid rotators—the core and envelope rotate with the same angular velocity
2. General rotational evolution is driven from angular momentum loss from the surface of the star as a result of the magnetic field and stellar wind. The wind braking prescription is adapted from [Lanzafame & Spada \(2015\)](#) and incorporates the mass-dependence from [Barnes & Kim \(2010\)](#) and the rotation rate dependence from [Kawaler \(1988\)](#).
3. Angular momentum can be exchanged between the core and the envelope.
4. The rotational coupling timescale—the typical timescale of angular momentum transport between the core and envelope—is mass dependent.

It is important to note that if a star experiences core-envelope decoupling during its rotational evolution then its period-age relationship will change. This has become increasingly clear through the recent work of [Curtis et al. \(2019\)](#) and [Curtis et al. \(2020\)](#) that showed open cluster sequences are rotating faster than expected. Including internal angular momentum transport between the core and envelope of a star could help to explain the faster-than-expected rotation periods, and it would also mean that current gyrochronology models, incorrectly estimate stellar ages. However, we do not yet have enough calibrators to robustly test models. It is especially important to extend gyrochronology relationships into the low-mass regime because there are few other ways to estimate the ages of these stars. The only way to improve gyrochronology models is to increase the number of low-mass calibrators—especially those that

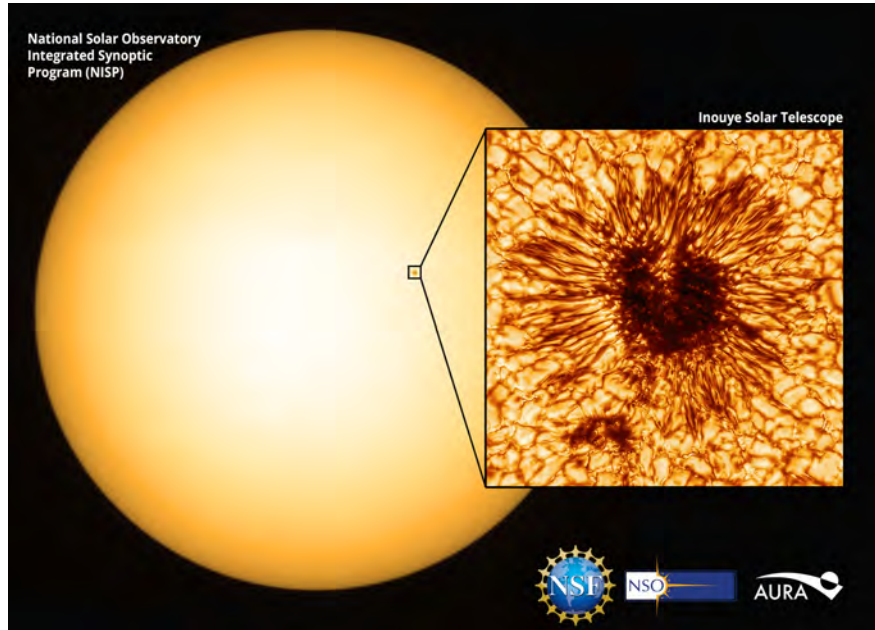


**Figure 3.** A high resolution image of the sun taken with the Daniel K. Inouye Solar Telescope. Dark colors on the image reflect the cooler areas of the solar surface. In zoomed-out images of the sun the surface often looks uniform, but here we can see the surface is covered in small brightness variations.

have intermediate-old ages—to better constrain the poorly understood late rotational evolution of low-mass stars and provide more reliable period-age relations.

#### 1.4. *Asteroseismology*

Not all stars are in open clusters, but we can take advantage of coeval binary systems where one component’s age can be measured. Asteroseismology, a method for learning information about stars through their observed oscillations, is an excellent tool for estimating stellar parameters in these systems. Stellar oscillations are pressure waves which cause small temperature and, thus, brightness changes (Brown & Gilliland 1994). High photometric precision is required to observe stellar oscillation frequencies which is most easily obtained from space (Soderblom 2010; Bedding 2014).

Stars effectively act as gaseous spheres and begin to oscillate when excited waves propagate through the stellar material (Bedding 2014). These stellar oscillations modes arise from the restoring force acting within a star (Bedding 2014; Brown & Gilliland

1994). The restoring force is simply a force that acts to bring a body back to an equilibrium position; in the case of stars, the restoring force works to restore hydrostatic equilibrium. There are two primary types of oscillation modes: pressure-modes or “p-modes” and gravity modes or “g-modes” (Bedding 2014; Brown & Gilliland 1994). P-modes are acoustic waves where the pressure gradient in a star is acting as the restoring force; g-modes are where buoyancy acts as the restoring force (Bedding 2014; Brown & Gilliland 1994). In stars like the Sun, p-mode oscillations are excited by motions of stellar material in the surface convection zone (Bedding 2014). Stars with solar-like oscillations must have surface temperatures cool enough to support a surface convection zone (Bedding 2014). The sun exhibits oscillations between 2500 to 4000  $\mu\text{Hz}$  with a power peak around 3100  $\mu\text{Hz}$ . Figure 4 shows the oscillation power spectrum for the Sun.

We can describe the motion of the stellar surface due to pulsations with spherical harmonics. For example, spherical harmonics allow each p-mode to be generalized to the radial order ( $n$ ), the angular degree ( $\ell$ ), and the azimuthal order ( $m$ ) (Bedding 2014; Brown & Gilliland 1994). The radial order specifies the number of nodal shells in the standing wave. The angular degree specifies the number of nodes at the surface of the star. For stellar oscillations not of the Sun, we expect to observe oscillation modes with  $\ell \leq 3$ . In the scope of this work the azimuthal order is not important, but the oscillation frequencies depend on  $m$  when the spherical symmetry of the star is broken. (Bedding 2014).

If we imagine a tuning fork, when the fork is struck it begins to vibrate. The vibrations create oscillations of high and low pressure regions—sound waves—which have frequencies that depend on the rate of the vibrations. The frequencies of stellar oscillations give insight to the pressure of the star which is proportional to the density (Bedding & Kjeldsen 2003). Further, fundamental stellar parameters, like age, mass,

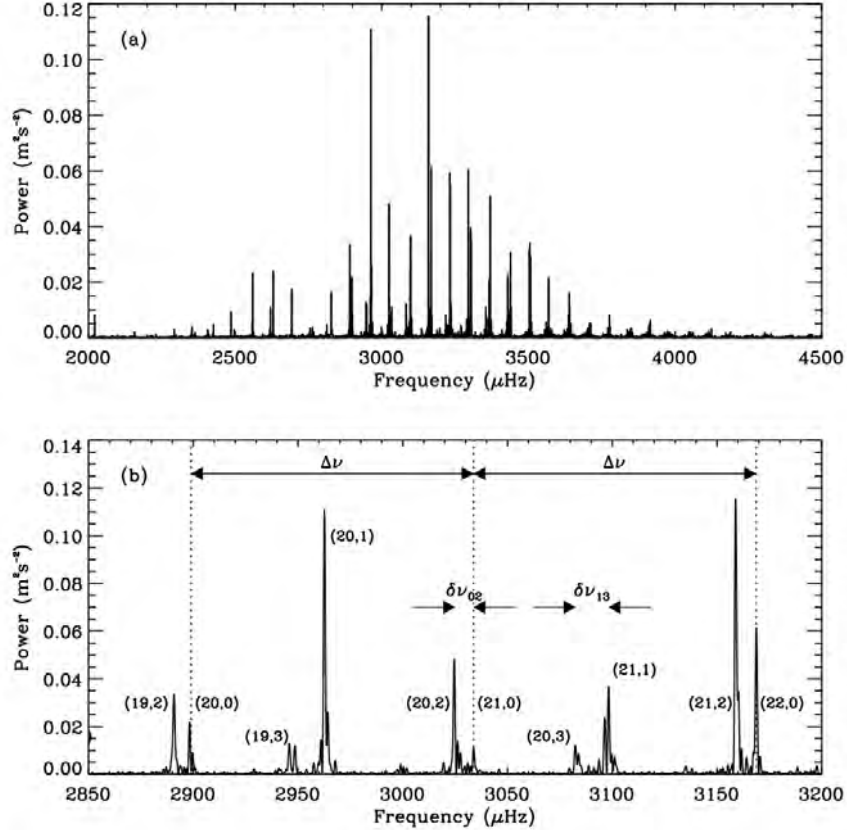


**Figure 4.** *Panel a:* The solar power spectrum from the BiSON instrument (see [Chaplin et al. \(1997\)](#)). *Panel b:* A zoom-in where each oscillation mode is labeled with its  $n$  and  $l$  values. From [Bedding \(2014\)](#).

and metal abundance, can be estimated by modeling the asteroseismic oscillation modes ([Bedding & Kjeldsen 2003](#); [Brown & Gilliland 1994](#); [Soderblom 2010](#)).

Two prominent features in asteroseismic detection are the “large” and “small” frequency separations. The large frequency separation,  $\Delta\nu$ , is the frequency spacing between modes of consecutive radial orders,  $n$ , but same degree  $l$  ([Bedding \(2014\)](#); [Brown & Gilliland \(1994\)](#)). The small frequency separation,  $\delta\nu$ , is the spacing between the  $l = 0$  and  $l = 2$  modes or the  $l = 1$  and  $l = 3$  modes for the same radial order ([Bedding 2014](#)). Physically,  $\Delta\nu$  is proportional to the square root of the mean stellar density, and  $\delta\nu$  is sensitive to the sound speed gradient near the core of the star and thus, the age ([Bedding 2014](#)).  $\Delta\nu$  is also commonly used when plotting asteroseismic

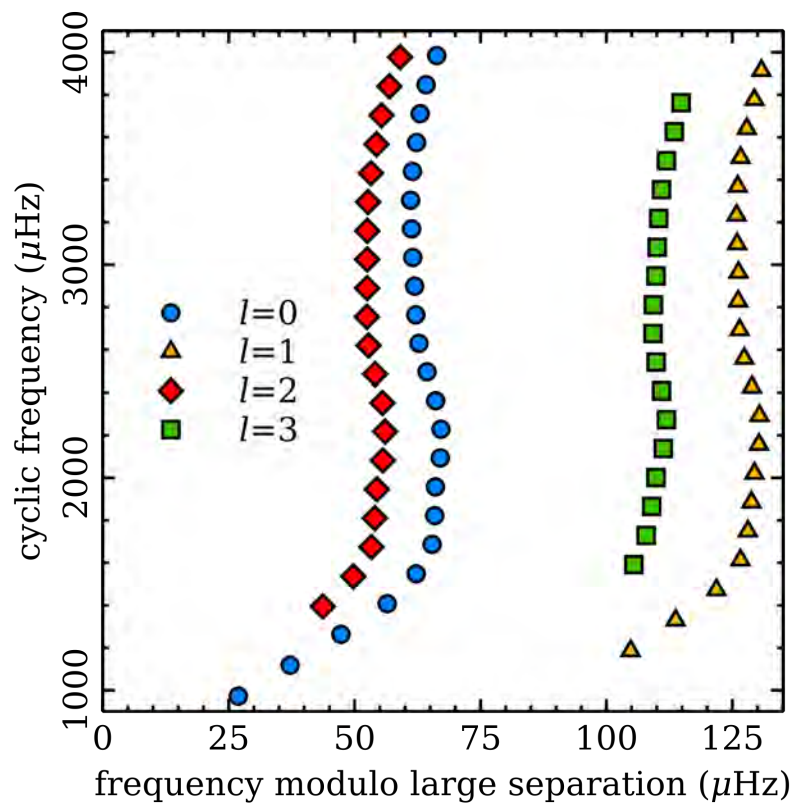


**Figure 5.** An échelle diagram of the low-order solar oscillation modes from the Birmingham Solar Oscillations Network (BiSON) observations (Broomhall et al. 2009; Davies et al. 2014) plotted by Dr. Warrick Ball.

information. Figure 4 shows the power frequency spectrum of the Sun with the large and small frequency separations labeled.

The échelle diagram, first used by [Grec et al. \(1983\)](#), plots the oscillation frequencies of a star, so the radial orders are ‘stacked’ vertically. Figure 5 shows an example of an échelle diagram diagram for the Sun. The x-axis of an échelle diagram is the frequency of a mode modulo  $\Delta\nu$ . The modulo operation, represented by %, takes the remainder of a division as the answer rather than the division itself. For example,  $3\%2 = 1$ ,  $4\%4 = 0$ ,  $10\%4 = 2$ . In general, the échelle diagram can be a convenient way to estimate  $\Delta\nu$  quickly by eye.

From asteroseismology, researchers have been able to learn detailed information about the solar interior such as how the sound speed (Christensen-Dalsgaard et al. 1985; Vorontsov 1989) and angular velocity (Duvall et al. 1984; Brown 1985; Brown et al. 1989; Libbrecht 1989) vary with depth and latitude, and estimate of depth of the solar convection zone (Christensen-Dalsgaard et al. 1991). Researchers have also been able to test long-standing problems in physics, such as the apparent solar neutrino deficit, frequency splitting as a result of stellar rotation, and frequency changes over the solar magnetic cycle (Brown & Gilliland 1994). The Sun has proven to be an invaluable resource for developing asteroseismology into a method for estimating fundamental stellar parameters. This opened the door for researchers, see Creevey et al. (2017), to measure *precise* ages for stars using asteroseismology. Thanks to precise long-cadence photometric observations from space-based missions like *Kepler* we can now apply these methods to thousands of new stars.

#### 1.4.1. *Kepler*

To do asteroseismology, we need high-cadence data with high photometric precision. The NASA *Kepler* mission was launched on March 6, 2009, with the primary goal of estimating how many Earth-like planets are in the habitable zone of solar-like stars (Borucki et al. 2010). The *K2* mission was proposed by the *Kepler* project in 2014 after the loss of two reaction wheels on the *Kepler* spacecraft (Howell et al. 2014). *K2*, unlike the original *Kepler* mission, focused pointing the telescope along the ecliptic, balancing the telescope against the solar radiation pressure so the remaining two reaction wheels could control pointing in two directions (Howell et al. 2014). This created observing campaigns of 75 days per field, which were downlinked at the end of each campaign (Howell et al. 2014).

*K2* also varies from the original *Kepler* mission in terms of data quality. Original measurements from Howell et al. (2014) showed that the *K2* spacecraft jitter was only a few percent larger than the three wheel *Kepler* mission. *K2*'s general photometric

performance was shown to be within a factor of 3-4 of the original *Kepler* mission's photometric precision, but the data must be further corrected for frequent position adjustments (Howell et al. 2014).

The *Kepler* and *K2* missions were pivotal in furthering our understanding of both stars and exoplanets. From NASA statistics, in the almost-decade of *Kepler* and *K2* operations, more than half a million stars were observed, and roughly 2,500 planets were confirmed around other stars<sup>1</sup>. The *Kepler* missions also produced an incredible amount of high-quality data for detecting oscillations in stars (Metcalf et al. 2017; Bedding 2014; Chaplin et al. 2010; Gilliland et al. 2010). The original *Kepler* mission added about 600 dwarf and subgiant stars to the asteroseismic sample and it is expected that the *K2* mission data will add between 100-200 more (Chaplin et al. 2014; Huber et al. 2013). Asteroseismic detections in red giant stars is a more recent development in asteroseismology, but between both *Kepler* missions, 10,000-30,000 new detections are expected in the coming years (de Assis Peralta et al. 2018; Yu et al. 2018).

## 2. PURPOSE

In this thesis, we report on a benchmark system for calibrating the M dwarf gyrochronology relationship. HIP 43232 is a wide binary system with near-solar metallicity comprised of an solar-like primary and an M dwarf secondary. We estimate the age of the binary system using asteroseismology and compare the rotation-age relationship of the M dwarf to current gyrochronology models. With a precise age and rotation period HIP 43232B becomes one of the first intermediate-aged calibrators for the M dwarf gyrochronology sample.

<sup>1</sup> See: <https://exoplanets.nasa.gov/keplerscience/>

### 3. SYSTEM INTRODUCTION

HIP43232 is a wide binary (Tokovinin 2014) with a projected angular separation of 34 arcseconds comprised of an F8V primary<sup>2</sup> and an M1.5V secondary (Montes et al. 2018). The primary has a metallicity near-solar of  $-0.03 \pm 0.07$  dex and an orbital period of 86 kilo-years (Montes et al. 2018; Tokovinin 2014). The primary and secondary have *Kepler* magnitudes of  $K_p = 8.8$  mag and  $K_p = 13.5$  mag respectively (Brown et al. 2011). The parallax of the system is  $\pi = 13.54 \pm 0.0454$  milli-arcseconds, which corresponds to a distance of  $73.85 \pm 0.25$  parsecs (Gaia Collaboration et al. 2018). Tokovinin (2014) estimates the masses of each component to be  $1.15 M_\odot$  and  $0.34 M_\odot$  for the primary and secondary, respectively. Finally, the effective temperature of the primary is estimated at  $T_{\text{eff}} = 6082 \pm 91$  K (Montes et al. 2018).

Using the Mann et al. (2015) relations,  $M_{K_s}$ , and  $[\text{Fe}/\text{H}]$ , we estimated the radius of the secondary to be  $0.420 \pm 0.021 R_\odot$ . Using  $M_{K_s}$  we estimated the mass of the secondary to be  $0.440 \pm 0.02 M_\odot$ . Using the Gaia BP-RP magnitude and  $[\text{Fe}/\text{H}]$ , we estimated the temperature of the secondary to be  $3421 \pm$  K. Finally, to account for the method-dependent systematic errors in the published  $T_{\text{eff}}$  and  $[\text{Fe}/\text{H}]$  measurement of the primary, we adopted a  $T_{\text{eff}}$  uncertainty of 1.5% (Tayar et al. 2020) and added in quadrature an uncertainty of 0.062 dex to the formal  $[\text{Fe}/\text{H}]$  uncertainty of 0.02 dex (Torres et al. 2012). A summary of parameters for each component in the system can be seen in Table 1.

In this thesis, we report on a benchmark system, HIP 43232, for calibrating the M dwarf gyrochronology relationship. We estimate the age of the binary system using asteroseismology and compare the rotation-age relationship of the M dwarf to current

<sup>2</sup> Note: Although the primary of this system is spectroscopically an F star, its properties make it analogous to the sun.

Stellar Parameters for HIP 42323A			
Parameter	HIP 43232A	Units	References
Spectral Type	F8V		Montes et al. (2018)
$T_{\text{eff}}$	$6082 \pm 91^{\dagger}$	K	Montes et al. (2018)
Radial Velocity	$3.63 \pm 0.05$	km/s	Montes et al. (2018)
$K_p$	$8.77 \pm 0.03$	mag	Huber et al. (2016)
$B_T$	$9.250 \pm 0.015$	mag	Høg et al. (2000)
$V_T$	$8.640 \pm 0.013$	mag	Høg et al. (2000)
BP	$8.7427 \pm 0.0015$	mag	Gaia Collaboration et al. (2018)
RP	$8.0245 \pm 0.0018$	mag	Gaia Collaboration et al. (2018)
J	$7.540 \pm 0.023$	mag	Cutri et al. (2003)
H	$7.308 \pm 0.059$	mag	Cutri et al. (2003)
K	$7.257 \pm 0.023$	mag	Cutri et al. (2003)
[Fe/H]	$-0.03 \pm 0.07^{\dagger}$	dex	Montes et al. (2018)
$\pi$	$13.652 \pm 0.0377$	mas	Gaia Collaboration et al. (2018)

Stellar Parameters for HIP 42323B			
Parameter	HIP 43232B	Units	References
Spectral Type	M1.5V		Montes et al. (2018)
$T_{\text{eff}}$	$3656 \pm 72$	K	Using Mann et al. (2015)
Radius	$0.420 \pm 0.021$	$R_{\odot}$	Using Mann et al. (2015)
Mass	$0.34, 0.440 \pm 0.02$	$M_{\odot}$	Tokovinin (2014), Using Mann et al. (2015)
$K_p$	$13.46 \pm 0.03$	mag	Huber et al. (2016)
$V_T$	15.16	mag	Tokovinin (2014)
BP	$15.1078 \pm 0.0015$	mag	Gaia Collaboration et al. (2018)
RP	$12.8004 \pm 0.0018$	mag	Gaia Collaboration et al. (2018)
J	$11.322 \pm 0.021$	mag	Cutri et al. (2003)
H	$10.756 \pm 0.030$	mag	Cutri et al. (2003)
K	$10.511 \pm 0.019$	mag	Cutri et al. (2003)

<sup>†</sup> Error values are the statistical and systematic errors estimates from Tayar et al. (2020) added in quadrature.

**Table 1.** A summary of stellar parameters for the A & B components of HIP 43232. The angular separation of the system is  $34.18 \pm 0.10$  arcsec and the orbital period is estimated to be 86.364 kilo-yrs.

gyrochronology models. With a precise age and rotation period HIP 43232B becomes one of the first intermediate-aged calibrators for the M dwarf gyrochronology sample.

## 4. ASTEROSEISMOLOGY

### 4.1. *Lightcurve Extraction*

HIP 42323 was observed in Campaigns 5 and 18 of the K2 mission (Howell et al. 2014). The late F star was observed in long cadence mode (30-minutes sampling) in both Campaigns 5 and 18. However, because solar-type stars oscillate on timescales of minutes, only the  $\sim 1$ -minute sampling utilized in Campaign 18 is useful for asteroseismology. The pixels on the Kepler CCD have an image scale of  $\sim 4$  arcsecond per pixel, meaning that the two components of this system are resolved individually (Howell et al. 2014). The two component system, clearly resolved, can be seen in Figure 6. Using the LightKurve<sup>3</sup> package, we created a mask that excluded the M dwarf flux to ensure there was no added signal (see Figure 6). We explored extracting both the Simple Aperture Photometry (SAP) and Pre-search Data Conditioning Simple Aperture Photometry (PDCSAP) flux from within the mask to find which gives the optimal signal-to-noise-ratio. The SAP flux is the sum of all the pixels within the aperture mask, meaning the flux can be affected by other astrophysical sources. The PDCSAP flux is the SAP flux corrected for instrumental variations. In this case, the optimal signal to noise ratio was achieved when using the SAP flux and our custom aperture mask rather than the pre-processed SAP and PDCSAP light curves.

After extracting the custom light curve, we normalized the light curve, removed any NaN values, and removed outliers greater than  $5\sigma$  from the mean. We create our final light curve using the corrected version of the light curve and the LightKurve implementation of the Self Flat Fielding (SFF) method from Vanderburg & Johnson (2014) with a window length of  $16 \mu\text{Hz}$  (Lightkurve Collaboration et al. 2018). SFF removes the short  $\sim 6$  hour ‘roll’ caused by the drifting of the K2 space craft by removing the correlation between the target pixel flux and the K2 spacecraft pointing

<sup>3</sup> LightKurve on GitHub: <https://github.com/KeplerGO/Lightkurve>

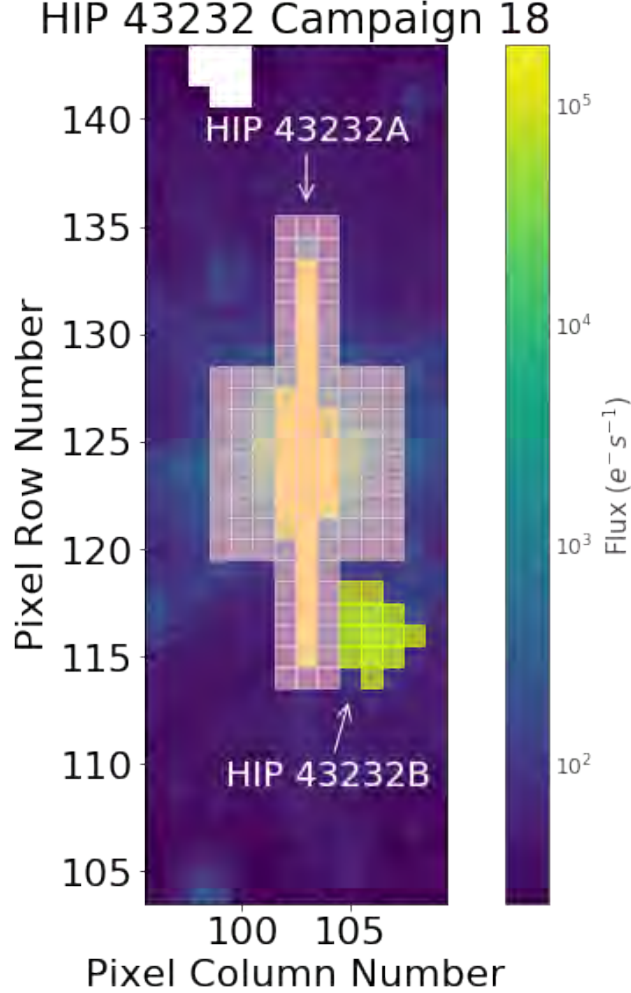


**Figure 6.** The K2 postage stamps for HIP43232 from both Campaign 18. The mask for HIP 43232B is a threshold mask where the included pixels must be  $3\sigma$  brighter than the median flux.

(Vanderburg & Johnson 2014). Finally, we calculated a power density spectrum by transforming the light curve using the Lomb-Scargle method (Lomb 1976; Scargle 1982; Lightkurve Collaboration et al. 2018).

#### 4.2. Frequency Modeling

Figure 7 shows the resulting power density spectrum on a log-log scale for HIP 43232A. We see power excess due to solar-like oscillations between 1900 and 3000  $\mu\text{Hz}$ , as well as a strong rise of power towards low frequencies due to convective granulation. The larger the radius of a star is, the lower its frequency range for solar-like

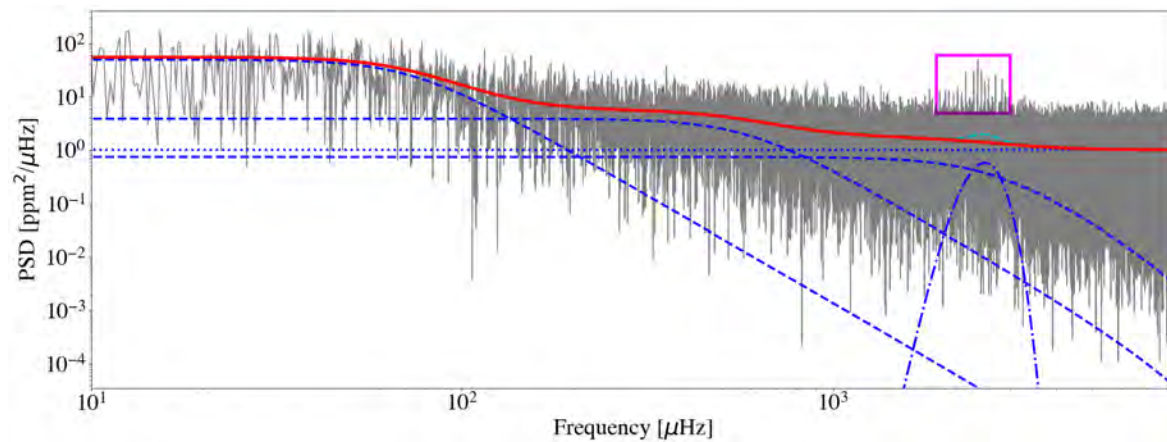


**Figure 7.** The power spectral density (PSD) of HIP43232A. The background fit (red line) is comprised of three Harvey-like profiles (dashed blue lines), a Gaussian envelope (dashed cyan line and dashed-dotted blue line), and the constant photon noise (dotted blue line). The frequency range is highlighted by a magenta box.

oscillations. HIP 43232A has a larger-than-solar radius<sup>4</sup>, and therefore oscillates at lower frequencies, in accordance with expectations from the equation for surface gravity ( $g \propto \frac{mass}{radius^2}$ ).

To model the granulation background and oscillation frequencies we used the high-Dimensional And multi-MOdal NesterD Sampling (DIAMONDS)<sup>5</sup> code. We first had to generate a background fit for the late F-type star (Corsaro & De Ridder 2014). DIAMONDS requires that we provide priors on several different types of parameter for a successful background fit: the constant noise component (in  $\text{ppm}^2/\mu\text{Hz}$ ), the amplitude of each Harvey component—a background noise spectrum component see Harvey (1985)—(in ppm, used to model convective granulation), the height of the oscillation envelope (in  $\text{ppm}^2/\mu\text{Hz}$ ), the width of the oscillation envelope (in  $\mu\text{Hz}$ ), and the frequency of maximum power (in  $\mu\text{Hz}$ ), for a 3-component granular background this results in 10 parameter-based-priors. We manually estimated the lower and upper limits of each parameter using a code that generates a rough background fit based on the median of the provided limits, which was provided by E. Corsaro. We quantified

<sup>4</sup> Note that the sun oscillates between 2500-4000  $\mu\text{Hz}$

<sup>5</sup> DIAMONDS on GitHub: <https://github.com/EnricoCorsaro/DIAMONDS>

NSMC Parameter	Value
Initial Live Points	500
Minimum Live Points	500
Maximum Draw Attempts	10000
Iterations without Clustering	1500
Iterations with Same Clustering	50
Initial Enlargement Fraction	2.10
Shrinking Rate	0.01
Termination Factor	0.01

**Table 2.** The NSMC hyperparameters used for successful Lorentzian profile fitting. For further clarification on these parameters can be found the [DIAMONDS Documentation](#).

the success of a DIAMONDS fit based on the marginal posterior distribution (MPD) for each parameter; an optimal MPD was considered to be Gaussian in shape. Figure 7 show the resulting best fit for each Harvey-like profile (dark blue dashed lines), the Gaussian envelope (cyan blue dashed lines), and the constant photon noise (dark blue dotted lines). The resulting background fit from combining each component is shown in red.

DIAMONDS models individual oscillation frequencies with a Lorentzian profile, which requires three different types of parameter-based-priors to be fit for each mode: the amplitude of each oscillation peak (in ppm), the central frequency of the oscillation peak (in  $\mu\text{Hz}$ ), and the line width of the oscillation peak (in  $\mu\text{Hz}$ ). Similar to the background fit, we manually estimated priors on the parameters for each Lorentzian profile using a code that generates rough profile fits based on the average of the input limits, provided by E. Corsaro. Other important DIAMONDS parameters that affect the efficiency of the search for the best fit model, such as the initial enlargement fraction of the ellipsoid sampler, were set using repeated experimentation and minor adjustments. The initial nested sampling Monte Carlo (NSMC) parameters can be found in Table 2.

Using this method we identified 19 *reliable*, low-degree modes between 1900 and 3000  $\mu\text{Hz}$  of orders  $\ell = 0, 1, 2$ . The final DIAMONDS combined Lorentzian profile fit can

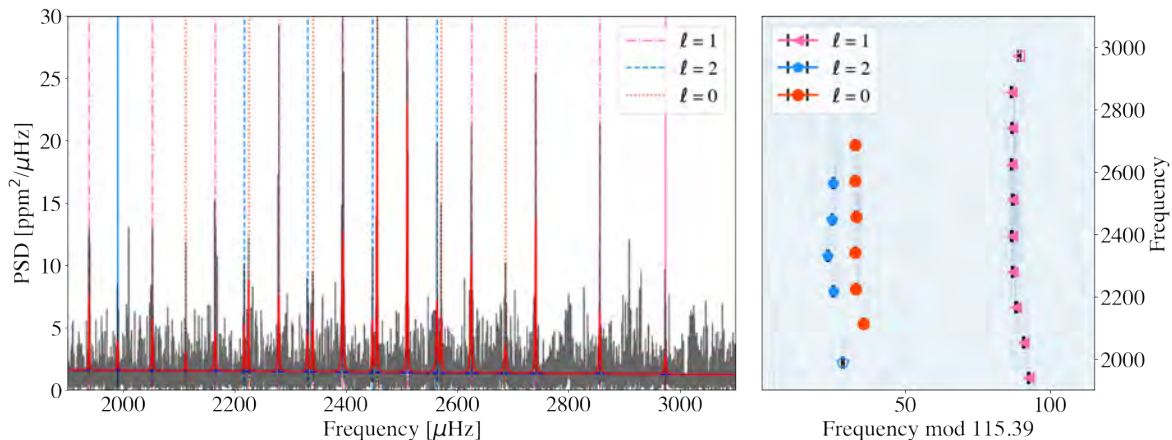


**Figure 8.** *Left Panel:* The background-corrected power density spectrum centered on of the p-mode frequency range. The range shown here is highlighted in magenta in Figure 7. The best peakbagging fit from DIAMONDS is shown in red. The mean background level is shown as the dashed blue line. Each mode except for two are marked by a vertical dashed, dot-dashed, or dotted line representing  $\ell = 2$ ,  $\ell = 1$ , or  $\ell = 0$  respectively. The other two modes are marked by solid vertical lines which are less reliable modes (see Section 4.2 for more detail). *Right Panel:* The échelle diagram in gray scale. The two less reliable modes are marked by open symbols. The p-modes of  $\ell = 0, 1, 2$  are represented by red-orange, hot pink, and dodger blue dots respectively on each graph.

be seen in Figure 8 (in red) with the accompanying échelle diagram. We identified two *unreliable* modes after DIAMONDS struggled to produce Gaussian-like MPDs after several successive runs, suggesting the modes may not be physical. This conclusion was supported by manual inspection of the échelle diagram, where the modes are not located in a shaded region, and the power frequency spectrum, where the modes are located in noisy areas. The modes, while not used in any stellar modeling discussed later, are included here for completeness. A summary of the final frequencies can be found in Table 3 and each mode’s width and amplitude can be found in Table 4.

### 4.3. Stellar Modeling

Before modeling the full set of asteroseismic frequencies to find the age of HIP 43232A we estimated ballpark values for fundamental stellar parameters such as mass, radius, and age using the Bellinger (2019) asteroseismic scaling relations. Input parameters and preliminary estimates are outlined in Table 5.

**Table 3.** The fitted mode frequencies for HIP43232A.

n	$\ell$	$\nu_{\ell,n} [\mu\text{Hz}]$	$\ell$	$\nu_{\ell,n} [\mu\text{Hz}]$	$\ell$	$\nu_{\ell,n} [\mu\text{Hz}]$
16	0	...	1	$1938.84^{+0.23}_{-0.23}$	2	...
17	0	...	1	$2052.52^{+0.30}_{-0.22}$	2	$1989.97^{+0.21}_{-0.53}$ †
18	0	$2112.52^{+0.35}_{-0.34}$	1	$2165.30^{+0.50}_{-0.33}$	2	...
19	0	$2225.27^{+0.15}_{-0.14}$	1	$2279.48^{+0.24}_{-0.22}$	2	$2217.51^{+0.28}_{-0.27}$
20	0	$2340.49^{+0.25}_{-0.36}$	1	$2394.60^{+0.26}_{-0.19}$	2	$2330.94^{+0.29}_{-0.38}$
21	0	$2456.11^{+0.20}_{-0.10}$	1	$2510.32^{+0.19}_{-0.14}$	2	$2447.79^{+0.21}_{-0.20}$
22	0	$2571.23^{+0.25}_{-0.27}$	1	$2625.27^{+0.17}_{-0.21}$	2	$2563.63^{+0.21}_{-0.28}$
23	0	$2686.56^{+0.58}_{-0.63}$	1	$2740.86^{+0.16}_{-0.17}$	2	...
24	0	...	1	$2856.08^{+0.29}_{-0.36}$	2	...
25	0	...	1	$2973.95^{+0.51}_{-0.39}$ †	2	...

† Excluded from stellar modeling, see the Section 4.2 for notes.

**Table 4.** The fitted amplitudes (A) and mode widths ( $\Gamma$ ) for the frequencies of HIP43232A.

n	$\ell$	$\Gamma [\mu\text{Hz}]$	A [ $\frac{\text{ppm}^2}{\mu\text{Hz}}$ ]	$\ell$	$\Gamma [\mu\text{Hz}]$	A [ $\frac{\text{ppm}^2}{\mu\text{Hz}}$ ]	$\ell$	$\Gamma [\mu\text{Hz}]$	A [ $\frac{\text{ppm}^2}{\mu\text{Hz}}$ ]
16	0	...	...	1	$1.139^{+0.31}_{-0.45}$	$4.73^{+0.60}_{-0.71}$	2	...	...
17	0	...	...	1	$1.96^{+0.44}_{-1.00}$	$5.13^{+0.62}_{-0.52}$	2	$1.72^{+0.41}_{-1.43}$ †	$3.33^{+0.65}_{-0.55}$ †
18	0	$1.40^{+0.69}_{-0.82}$	$2.58^{+0.57}_{-0.65}$	1	$2.81^{+0.70}_{-1.19}$	$5.35^{+0.50}_{-0.60}$	2	...	...
19	0	$1.00^{+0.28}_{-0.79}$	$4.65^{+0.75}_{-0.64}$	1	$2.04^{+0.59}_{-0.67}$	$6.41^{+0.61}_{-0.75}$	2	$1.31^{+0.35}_{-0.54}$	$4.04^{+0.64}_{-0.66}$
20	0	$1.77^{+0.44}_{-0.47}$	$4.91^{+0.53}_{-0.58}$	1	$2.32^{+0.44}_{-0.52}$	$9.43^{+0.54}_{-0.76}$	2	$2.02^{+0.59}_{-0.79}$	$4.48^{+0.56}_{-0.66}$
21	0	$1.07^{+0.30}_{-0.33}$	$8.59^{+0.75}_{-1.13}$	1	$1.33^{+0.26}_{-0.29}$	$9.87^{+0.72}_{-0.80}$	2	$1.67^{+0.54}_{-0.84}$	$4.76^{+0.53}_{-0.63}$
22	0	$2.17^{+0.48}_{-1.10}$	$5.56^{+0.66}_{-0.59}$	1	$2.38^{+0.43}_{-0.68}$	$8.65^{+0.61}_{-0.55}$	2	$2.44^{+0.61}_{-0.61}$	$6.88^{+0.93}_{-0.60}$
23	0	$3.89^{+1.01}_{-0.36}$	$5.60^{+0.66}_{-0.59}$	1	$1.50^{+0.42}_{-0.58}$	$7.99^{+0.67}_{-0.84}$	2	...	...
24	0	...	...	1	$2.30^{+0.64}_{-0.23}$ †	$6.29^{+0.56}_{-0.57}$ †	2	...	...
25	0	...	...	1	$2.77^{+0.68}_{-0.58}$	$4.04^{+0.46}_{-0.72}$	2	...	...

† Excluded from stellar modeling, see the end of Section 4.2 for notes.

To improve the accuracy of the age estimate, we performed detailed modelling of the oscillation frequencies using the Modules for Experiments in Stellar Astrophysics (MESA)<sup>6</sup> stellar evolution code. MESA is open source, adaptable, and continuously under development to allow the stellar astrophysics community to test new physics as it

<sup>6</sup> MESA Home: <http://mesa.sourceforge.net/index.html>

Parameter	Value	Ref.
$\Delta\nu$	$115.12 \pm 0.19 \mu\text{Hz}$	This work
$\delta\nu$	$8.30 \pm 0.39 \mu\text{Hz}$	This work
$\nu_{\text{max}}$	$2456.15_{-0.10}^{+0.20} \mu\text{Hz}$	This work
[Fe/H]	$-0.03 \pm 0.07^\dagger$	Montes et al. (2018)
$T_{\text{eff}}$	$6028 \pm 91^\dagger \text{ K}$	Montes et al. (2018)
From the Bellinger (2019) Scaling Relation		
Mass	$1.052 \pm 0.030 M_\odot$	
Radius	$1.129 \pm 0.010 R_\odot$	
Age	$4.49 \pm 0.51 \text{ Gyr}$	

<sup>†</sup> Error values are changed from their original citations, see notes in paragraph two of Section 3.

**Table 5.** A summary of input parameters, above the solid line, and output parameters, below the solid line, from the Bellinger (2019) scaling relation.

arises. The current MESA capabilities are outlined in Paxton et al. (2011, 2013, 2015, 2018, 2019).

In our model (A), we adopt a standard set of input physics for the underlying MESA models. We adopted the solar chemical mixture from Grevesse & Sauval (1998), with the opacity tables from Iglesias & Rogers (1996) supplemented with the low temperature opacities of (Ferguson et al. 2005). We treat both helium and heavy element diffusion according to the Thoul et al. (1994) prescription. We adopt the JINA Recalib nuclear reaction rates (Cyburt et al. 2010).

We utilized the MESA `astero` module (Paxton et al. 2013) coupled with the GYRE (Townsend & Teitler 2013) oscillation code to calculate model frequencies and search for the best fit to our observed oscillation modes. The calculation of oscillation frequencies requires the structure variables in the atmosphere, so we used an opacity varying Eddington Gray  $T(\tau)$  relation coupled with a asteroseismic surface term correction using the cubic method of Ball & Gizon (2014). We implemented the Nelder-Mead simplex method (J.A. Nelder & R. Mead 1965) from the `astero` module to search for the best-fit model.

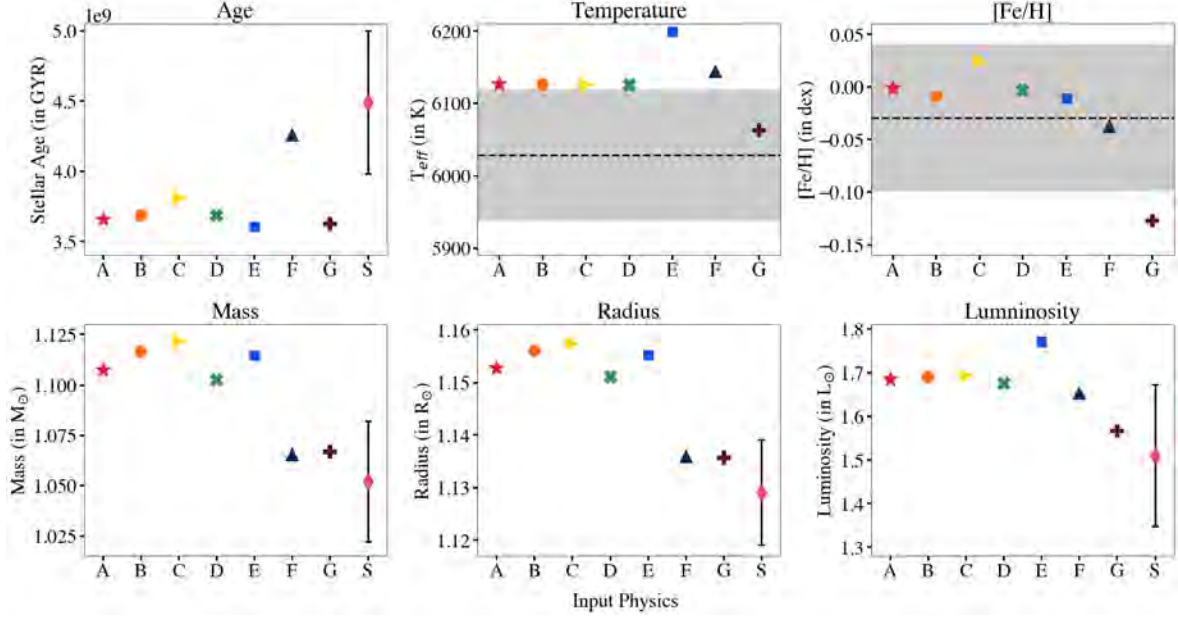


**Figure 9.** Key output parameters based on MESA input physics variations. The labeling of each parameter corresponds to the input physics discussed in Section 4.3.1. 4 graphs contain an additional point labeled ‘S’ corresponding to the results in Table 5 for comparison. The 2 other graphs have the spectroscopic constraints from Table 1 for comparison.

In each run  $[\text{Fe}/\text{H}]$ , mass, and the mixing length parameter,  $\alpha$ , were varied. Only effective temperature and  $[\text{Fe}/\text{H}]$  were used as spectroscopic constraints. We assumed a fixed chemical enrichment law with  $dy/dz = 1.4$ ; helium was not allowed to vary independently. The  $\chi^2$  value for each run weighted asteroseismic constraints heavier than spectroscopic constraints with an 80/20 split. This encouraged MESA to focus on fitting the asteroseismic frequencies well, using temperature and  $[\text{Fe}/\text{H}]$  as looser constraints.

#### 4.3.1. Parameter Variations

It is well known that inferred stellar parameters vary with the assumed input physics (see [Tayar et al. \(2020\)](#) for a recent detailed example). Formal errors on MESA model results tend to be small due to the precision of the oscillation frequencies, but do not capture the systematic errors stemming from the choice of input physics. In order to better understand the true error budget we tried several physics variations to gauge how

Variation	Age (in Gyr)	Mass (in $M_{\odot}$ )	Radius (in $R_{\odot}$ )	T (in K)	Surface Luminosity (in $L_{\odot}$ )	Initial Fe/H (in dex)	$\alpha$
A	3.809	1.122	1.151	6125	1.676	-0.003	1.939
B	3.684	1.117	1.156	6126	1.690	-0.009	1.947
C	3.809	1.122	1.157	6125	1.694	0.025	1.901
D	3.684	1.103	1.151	6126	1.676	-0.003	1.943
E	3.601	1.115	1.155	6199	1.771	-0.011	2.468
F	4.262	1.065	1.136	6145	1.652	-0.037	1.803
G	3.622	1.067	1.136	6063	1.566	-0.127	1.689

**Table 6.** A summary of results for each parameter variation model. Model A uses the input physics described in Section 4.3. Model B and C use different values for  $dy/dz$  based off of solar calibrations using the Grevesse & Sauval (1998) or the Asplund et al. (2009) oxygen abundances, respectively. Model D uses the OP opacity tables. Model E trades the Eddington Gray for the Krishna Swamy boundary condition. In Model F we turned elemental diffusion off. Lastly, in Model G we used the Kjeldsen et al. (2008) surface correction.

the output stellar parameters changed. We modeled six additional parameter variations to understand how the output for important stellar parameters would change.

We started by using MESA to model the Sun using the input physics described in Section 4.3. Using the solar model we found the value for the rate that the helium abundance in a star changes with respect to the metallicity of a star,  $dy/dz$ , to be 1.05. In the first parameter variation (B), we replaced the original rate with  $dy/dz = 1.05$  and held it fixed throughout the run. For the next variation (C), we again used a solar model to find  $dy/dz$ , but changed the Grevesse & Sauval (1998) oxygen abundance to that from Asplund et al. (2009) and adopted the appropriate opacity tables to account for the change in the abundance pattern. We then used the new  $dy/dz$  from a solar model calibrated with the Asplund et al. (2009) abundances and appropriate opacity tables with the other input physics described in 4.3 to model the star. Asplund et al. (2009) finds a notably lower values for the oxygen abundance which lowers the inferred opacity at the base of the solar convective zone. In the each of the subsequent physics variations aside from A and B, we elected to use  $dy/dz = 1.4$ .

In the third variation (D), we changed the opacity tables from OPAL (Iglesias & Rogers 1996) to OP tables (Seaton et al. 1994). In the next variation (E), we changed the boundary from the Eddington Gray to the Krishna Swamy condition (Krishna Swamy 1966). Then, in (F), we turned off elemental diffusion and gravitational settling. In the final variation (G), we changed the surface correction from Ball & Gizon (2014) to Kjeldsen et al. (2008). Each parameter variation used the same Nelder-Mead simplex method from the `astero` module to search for the best-fit model. The resulting output for each parameter variation are summarized in Table 6 and visually in Figure 9.

From Figure 9 we can easily see that the first 4 physics variations, models B, C, D, and E, all have similar results for key parameters. These models tend to fall outside of the values predicted from the scaling relation for age mass, radius, and luminosity—trending higher than predicted for all but the age. Generally the models agree well with the spectroscopic constraints being both close to the observed temperature and Fe/H value, with the exception of model E with the hottest temperature and model G with the lowest metallicity. Interestingly, model F, where elemental diffusion was neglected, agrees the best with both the scaling relation values and the spectroscopic constraints, falling within the error bars for all of the key parameters except the temperature.

## 5. STELLAR ROTATION OF THE LOW-MASS COMPANION

HIP43232B was observed with both K2 and Zwicky Transient Factory (ZTF). ZTF is a ground-based time-domain survey that started in 2017 at the Palomar Observatory. The time overlap of all of the light curves can be seen in Figure 10.

### 5.1. *Lightcurve Preparation*

The K2 light curves were corrected differently from the method outlined in Section 4.2 because the SFF method from Vanderburg & Johnson (2014) is known to remove long-term periodic trends which we expected to see in the light curve for the M dwarf. Instead, we opted to use the Lightkurve implementation of Pixel Level Decorrelation (PLD) based on Deming et al. (2015), which was adapted for use on K2 by Luger et al.

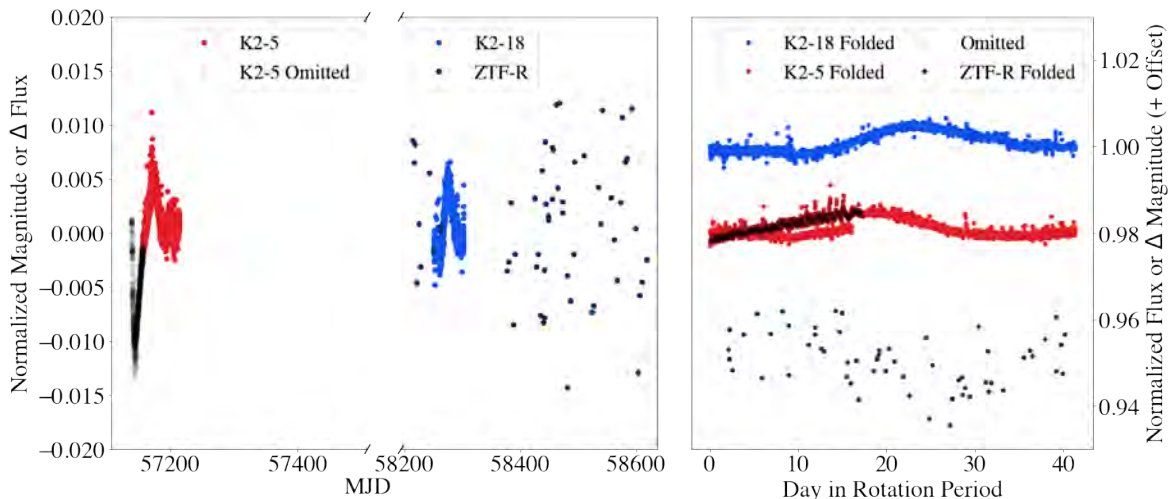


**Figure 10.** *Top:* The time overlap of all the light curves for HIP 43232B. *Bottom:* All of the light curves phased with the period determined using the ZTF light curve.

(2016) and Luger et al. (2018). When implementing PLD, we were careful to choose a PLD aperture which did not contain the strip of saturated pixels from HIP3232A, seen in Figure 6, to ensure we only saw the signal from HIP3232B. The light curve from Campaign 5 contained an artifact—likely poorly corrected instrumental behavior, also noted in Esselstein et al. (2018). As a result, we elected to remove the first 800 cadences of the campaign to remove any rotation period bias they might cause. Finally, we transformed the light curve into a periodogram using the Lomb-Scargle method using a standard over-sample factor of 5 to display the full features of the power spectrum and took the maximum peak as the most likely period for each light curve.

The method of creating the ZTF light curve was similar to that outlined for the light curves created using the Palomar Transient Factory data in Curtis et al. (2020). Each image has a  $47^\circ \times 47^\circ$  field of view and on average 3750 square degrees are covered in a single hour to a depth of 20.5 mag. HIP 43232B was observed over two main ZTF seasons with coverage starting in September 2018 and ending in May 2019.

To improve the photometric precision of the light curve, local differential photometry was performed in the vicinity of HIP 43232B. Differential photometry measures the difference in brightness between two objects; here, reference sources are assumed to be

Survey	Period
K2 Campaign 5	$47.8 \pm 4.8$ days
K2 Campaign 18	$36.3 \pm 3.6$ days
ZTF r-Band	$41.3 \pm 4.1$ days

**Table 7.** The estimation of the M dwarf rotation period for each light curve. The error bar on each period follows [Epstein & Pinsonneault \(2014\)](#).

constant while our target varies with time due to spot modulation. Calibrated ZTF images were downloaded from the NASA/IPAC Infrared Science Archive (IRSA)<sup>7</sup>. We found all stars within  $\pm 1.5$  mag of HIP 43232B in the same image and performed simple aperture photometry on all of these stars for every image. We created a systematic photometric zero-point light curve by subtracting off the median magnitude of each star and median combining the results for each star. To produce the final light curve, we subtracted off this signal from our initial light curve. There were two filters for the ZTF light curves, r- and g-band; r-band was significantly less noisy so it was used to estimate the period. The light curve was transformed into a periodogram using the Lomb-Scargle method with an over-sample factor of 20 and the maximum peak was taken as the most likely period. We use a higher over-sample factor here because the ZTF light curve is so sparsely sampled.

## 5.2. Rotation Period Measurement

The ZTF light curve was comprised of far fewer points than either of the K2 light curves, to ensure the estimated period was significant we calculated the false alarm probability. To estimate the false alarm probability (the probability that the rotation period is not due to white noise) the y-values of the light curve were randomly scrambled among the x-values and the scrambled light curve was transformed into a periodogram. This process was repeated 10000 times and the periodograms from each run were over-

<sup>7</sup> <https://irsa.ipac.caltech.edu/applications/ztf/>

Model	Estimated Period	Comment
<a href="#">Barnes &amp; Kim (2010)</a>	60.02 days	Empirical
<a href="#">Angus et al. (2019)</a>	61.88 days	Empirical
<a href="#">Spada &amp; Lanzafame (2020)</a>	33.94 days	Core-Envelope Decoupling

**Table 8.** The estimation of the M dwarf rotation period from various models.

plotted with the original ZTF-r band periodogram. From this we found the rotation period from the ZTF r-band light curve had a low false alarm probability of  $\sim 0.14\%$ .

With the two K2 light curves we found rotation periods of 47.8 and 36.3 days for Campaigns 5 and 18, respectively. The ZTF-r light curve predicts a rotation period roughly halfway between the two K2 Campaign periods at 41.3 days. Table 7 summarizes the periods observed from each of the light curves. We adopt the ZTF-r period as the rotation period of HIP 43232B because the light curve covers more rotation cycles of the star.

## 6. DISCUSSION

Using asteroseismology and stellar modeling of HIP 43232A we estimate the age of the system HIP 43232 to be between  $\sim 3.6 - 4.3$  Gyr. From the [Mann et al. \(2015\)](#) relations we were able to estimate that HIP 43232B has a mass of  $0.44 \pm 0.02 M_{\odot}$ , a radius of  $0.42 \pm 0.021 R_{\odot}$ , a temperature of  $3656 \pm 72$  K, and a rotation period of  $\sim 42$  days. In this discussion we explore how the observed rotation of HIP 43232B compares to current gyrochronology models.

M dwarfs are structurally and magnetically distinct from solar-like stars, and thus, we have little reason to assume that solar-calibrated models extrapolated to the low-mass regime will perform particularly well. Both empirical and theoretical models lack low-mass calibrators that would improve rotation estimates—especially at mid-older ages. Figure 11 illustrates the true lack of rotational evolution calibrators in the same regime as HIP 43232B. The color-rotation space that HIP 43232B occupies is entirely unconstrained by well calibrated rotation relationships from open clusters and only

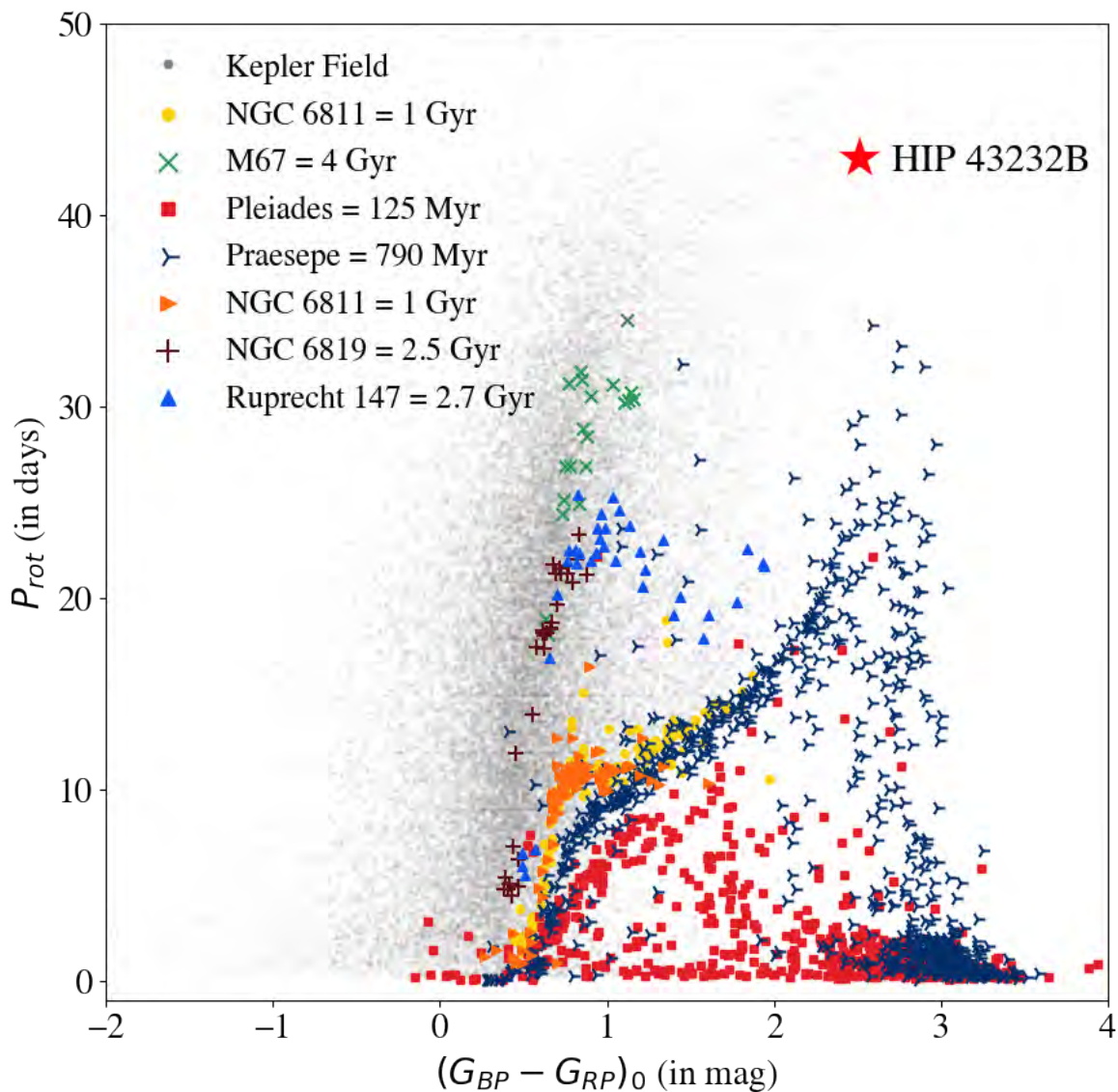


**Figure 11.** A comparison of well studied open clusters with precise ages and rotation periods overlaid on the Kepler field featuring the age and rotation period of HIP 43232B. References in legend order: [McQuillan et al. \(2014\)](#), [Curtis et al. \(2019\)](#), [Barnes et al. \(2016\)](#), [Rebull et al. \(2016\)](#), [Rebull et al. \(2017\)](#), [Meibom et al. \(2011\)](#), [Meibom et al. \(2015\)](#), and [Curtis et al. \(2020\)](#). HIP 43232B sits in a particularly interesting and unexplored area of this graph being outside of the areas well covered by the open clusters.

sparsely sampled in the Kepler field. Recent works from [Curtis et al. \(2020\)](#); [Gruner & Barnes \(2020\)](#); [Curtis et al. \(2019\)](#); [Agüeros et al. \(2018\)](#); [Douglas et al. \(2016\)](#) and [Delorme et al. \(2011\)](#) show that gyrochronology relationships extrapolated from higher mass stars in intermediate aged clusters, such as those shown in Figure 11, over-estimate the rotation period of low-mass stars.

Using Table 1 in [Barnes & Kim \(2010\)](#), we interpolated between 0.4 and 0.45  $M_{\odot}$  to find the corresponding global convective turnover timescale,  $\tau_c$ , for the mass of HIP 43232B. Using the constants  $P_0 = 1.1$  days and  $k_I = 452$  Myr/day, and Equation 9 from [Barnes \(2010\)](#) we find the empirical relationship from [Barnes & Kim \(2010\)](#) predicts a 60.019 day rotation period for HIP 43232B. To find the rotation period estimated from the [Angus et al. \(2019\)](#), we used the `gyro_model_praesepe` module in the `stardate` package using, Gaia color, and the age of HIP 43232 from MESA Model A as constraints. Using the [Angus et al. \(2019\)](#) relations, we estimated the rotation period of HIP 43232B to be 61.88 days. The results from [Barnes & Kim \(2010\)](#) and [Angus et al. \(2019\)](#) are consistent with the trend that empirically calibrated models extrapolated to low-mass regimes largely over predict the observed rotation period for low-mass stars.

We also compare the observed rotation period and age of HIP 43232B to the [Spada & Lanzafame \(2020\)](#) observationally calibrated theoretical rotation model, which allows for internal differential rotation and angular momentum transport. The rotational coupling timescale and wind-braking prescriptions used in [Spada & Lanzafame \(2020\)](#) are both strongly mass-dependent ([Lanzafame & Spada 2015](#); [Somers & Pinsonneault 2016](#)). The model predicts that while a PMS is fully convective it rotates as a solid body. As the star contracts, it begins to develop a radiative core and braking from magnetic wind reaches maximum efficiency, spinning down the envelope. As the differential rotation continues, the braking efficiency declines, and the rate of angular momentum loss from the envelope and transfer from the core balance each other, making it appear that the star stalls in its spin down or continues to rotate at a constant rate. Eventually, the core and envelope re-couple rotationally, and the star begins to spin as a solid body again. For a more comprehensive review and visualizations of core-envelope decoupling refer to Section 1.3. In stars with masses less than solar, the above process is emphasized because the re-coupling timescales are long, and can

impact the rotational evolution for gigayears. [Spada & Lanzafame \(2020\)](#) theorize that core-envelope decoupling becomes significant for stars around  $0.5M_{\odot}$  several Gyr into their lifetimes, the relevant regime for HIP 43232B.

HIP 43232B is  $\sim 3.6$  Gyr star with an observed rotation period  $\sim 20$  days faster than predicted by standard models. The [Spada & Lanzafame \(2020\)](#) model predicts a faster rotation period than what was observed for HIP 43232B, 33.94 days. The predicted rotation period from [Spada & Lanzafame \(2020\)](#) is over 10 days closer to the actual rotation period of HIP 43232B than the next closest model from [Barnes & Kim \(2010\)](#). However, even with the inclusion of core-envelope decoupling, the estimated rotation period is still  $2\sigma$  away from the observed period. This may suggest there are other factors affecting in rotational spin down that gyrochronology models fail to account for or that the assumed mass dependence and coupling timescales are incorrect. Using a single star, it is impossible to extrapolate a common core-envelope decoupling timescale for all low-mass stars, although, this study of HIP 43232B does support that such a scenario may exist. With more observational anchors we can test the rotational decoupling timescale and add new calibrators to test gyrochronology models in the low mass regime.

## 7. CONCLUSION

We characterized the wide binary system HIP 43232 by modeling the solar-like oscillations of HIP 43232A. Using light curves of HIP 43232B, we estimated a rotation period and compared the age-rotation relationship to current gyrochronology models. Our main take-aways of the system are as follows:

- HIP 43232A is an F8V star observed in Campaigns 5 and 18 of K2. Using asteroseismic and spectroscopic constraints we modeled HIP 43232A using MESA finding an age between  $\sim 4.3$  and  $3.6$  Gyr, radius between  $\sim 1.16$  and  $\sim 1.15 R_{\odot}$ , and mass between  $\sim 1.12$  and  $\sim 1.07 M_{\odot}$ .

- Using K2 and supplementary data from ZTF, we measure the rotation period of HIP 43232B to be  $P_{\text{rot}} = 41.3 \pm 4.1$  days. This makes HIP 43232B one of the first middle-aged M dwarf gyrochronology calibrators.
- We used the asteroseismic age from HIP 43232A to estimate rotation periods of HIP 43232B using models from Barnes & Kim (2010) ( $P_{\text{rot}} \sim 60$  days), Angus et al. (2019) ( $P_{\text{rot}} \sim 62$  days), and Spada & Lanzafame (2020) ( $P_{\text{rot}} \sim 33.94$  days). Of these the rotation periods, the Spada & Lanzafame (2020) core-envelope decoupling model comes closest to predicting the actual rotation period of HIP 43232B with a difference of  $\sim 8$  days.
- The observed rotation period is more consistent with models that allow for internal angular momentum transport, resulting in a prolonged M dwarf spin-down stall timescale.

HIP 43232 gives insight into a previously unconstrained area of M dwarf spin-down. However, more old-aged M dwarf gyrochronology calibrators are essential to improving our understanding of the low-mass spin-down timescale. The first release from Gaia DR3 has already added several new binary systems with low-mass companions that can be used to further investigate low-mass gyrochronology. Systems like these can be observed with the Transiting Exoplanet Survey Satellite and similar analyses to those in this thesis can be used to characterize key parameters about each system, providing more calibrators for gyrochronology. In the longer-term future, gyrochronology relationships will be greatly improved by observations from the proposed PLANetary Transits and Oscillations of stars (PLATO) mission. PLATO's primary goal is to understand planetary habitability through detecting planets, estimating planetary parameters, and finding the relationship between planets and their host stars. In particular, PLATO will use asteroseismology to determine accurate stellar parameters. The future holds several exciting opportunities for improving the understanding of angular

momentum loss and transport in stars, constraining the rotational decoupling timescale for low-mass stars, and bettering our understanding of stellar rotational evolution.

## SCIENCE ACKNOWLEDGEMENTS

This research would not have been possible without all of the hard working engineers & scientists that developed instruments, data processing tools, web interfaces, and software below:

*Facilities:* ATLAS, MAST, Kepler, Gaia, ZTF

*Software:* DIAMONDS (Corsaro & De Ridder 2014), echelle (Hey & Ball 2020), GYRE (Townsend & Teitler 2013), Lightkurve (Lightkurve Collaboration et al. 2018), MESA (Paxton et al. 2011, 2013, 2015, 2018, 2019), matplotlib (Hunter 2007), numpy (Harris et al. 2020), scipy (Virtanen et al. 2020), pandas (The Pandas Development Team 2020; Wes McKinney 2010)

## REFERENCES

- Abt, H. A. 1983, *ARA&A*, 21, 343, doi: [10.1146/annurev.aa.21.090183.002015](https://doi.org/10.1146/annurev.aa.21.090183.002015)
- Adams, F. C., & Laughlin, G. 1997, *Reviews of Modern Physics*, 69, 337, doi: [10.1103/RevModPhys.69.337](https://doi.org/10.1103/RevModPhys.69.337)
- Aerts, C., Mathis, S., & Rogers, T. M. 2019, *ARA&A*, 57, 35, doi: [10.1146/annurev-astro-091918-104359](https://doi.org/10.1146/annurev-astro-091918-104359)
- Agüeros, M. A., Bowsher, E. C., Bochanski, J. J., et al. 2018, *ApJ*, 862, 33, doi: [10.3847/1538-4357/aac6ed](https://doi.org/10.3847/1538-4357/aac6ed)
- Angus, R., Morton, T. D., Foreman-Mackey, D., et al. 2019, *AJ*, 158, 173, doi: [10.3847/1538-3881/ab3c53](https://doi.org/10.3847/1538-3881/ab3c53)
- Angus, R., Beane, A., Price-Whelan, A. M., et al. 2020, *AJ*, 160, 90, doi: [10.3847/1538-3881/ab91b2](https://doi.org/10.3847/1538-3881/ab91b2)
- Asplund, M., Grevesse, N., Sauval, A. J., & Scott, P. 2009, *ARA&A*, 47, 481, doi: [10.1146/annurev.astro.46.060407.145222](https://doi.org/10.1146/annurev.astro.46.060407.145222)
- Ball, W. H., & Gizon, L. 2014, *A&A*, 568, A123, doi: [10.1051/0004-6361/201424325](https://doi.org/10.1051/0004-6361/201424325)
- Barnes, S. A. 2003, *ApJ*, 586, 464, doi: [10.1086/367639](https://doi.org/10.1086/367639)
- . 2007, *ApJ*, 669, 1167, doi: [10.1086/519295](https://doi.org/10.1086/519295)
- . 2010, *ApJ*, 722, 222, doi: [10.1088/0004-637X/722/1/222](https://doi.org/10.1088/0004-637X/722/1/222)
- Barnes, S. A., & Kim, Y.-C. 2010, *ApJ*, 721, 675, doi: [10.1088/0004-637X/721/1/675](https://doi.org/10.1088/0004-637X/721/1/675)
- Barnes, S. A., Weingrill, J., Fritzewski, D., Strassmeier, K. G., & Platais, I. 2016, *ApJ*, 823, 16, doi: [10.3847/0004-637X/823/1/16](https://doi.org/10.3847/0004-637X/823/1/16)
- Bedding, T. R. 2014, *Solar-like oscillations: An observational perspective*, ed. P. L. Pallé & C. Esteban, 60
- Bedding, T. R., & Kjeldsen, H. 2003, *PASA*, 20, 203, doi: [10.1071/AS03025](https://doi.org/10.1071/AS03025)
- Bellinger, E. P. 2019, *MNRAS*, 486, 4612, doi: [10.1093/mnras/stz714](https://doi.org/10.1093/mnras/stz714)
- Borucki, W. J., Koch, D., Basri, G., et al. 2010, *Science*, 327, 977, doi: [10.1126/science.1185402](https://doi.org/10.1126/science.1185402)
- Broomhall, A. M., Chaplin, W. J., Davies, G. R., et al. 2009, *MNRAS*, 396, L100, doi: [10.1111/j.1745-3933.2009.00672.x](https://doi.org/10.1111/j.1745-3933.2009.00672.x)
- Brown, T. M. 1985, *Nature*, 317, 591, doi: [10.1038/317591a0](https://doi.org/10.1038/317591a0)
- Brown, T. M., Christensen-Dalsgaard, J., Dziembowski, W. A., et al. 1989, *ApJ*, 343, 526, doi: [10.1086/167727](https://doi.org/10.1086/167727)
- Brown, T. M., & Gilliland, R. L. 1994, *ARA&A*, 32, 37, doi: [10.1146/annurev.aa.32.090194.000345](https://doi.org/10.1146/annurev.aa.32.090194.000345)
- Brown, T. M., Latham, D. W., Everett, M. E., & Esquerdo, G. A. 2011, *AJ*, 142, 112, doi: [10.1088/0004-6256/142/4/112](https://doi.org/10.1088/0004-6256/142/4/112)
- Chaplin, W. J., Elsworth, Y., Isaak, G. R., et al. 1997, *MNRAS*, 288, 623, doi: [10.1093/mnras/288.3.623](https://doi.org/10.1093/mnras/288.3.623)
- Chaplin, W. J., Appourchaux, T., Elsworth, Y., et al. 2010, *ApJL*, 713, L169, doi: [10.1088/2041-8205/713/2/L169](https://doi.org/10.1088/2041-8205/713/2/L169)
- Chaplin, W. J., Kjeldsen, H., Bedding, T. R., et al. 2011, *ApJ*, 732, 54, doi: [10.1088/0004-637X/732/1/54](https://doi.org/10.1088/0004-637X/732/1/54)
- Chaplin, W. J., Basu, S., Huber, D., et al. 2014, *ApJS*, 210, 1, doi: [10.1088/0067-0049/210/1/1](https://doi.org/10.1088/0067-0049/210/1/1)
- Chapman, S., Pongracic, H., Disney, M., et al. 1992, *Nature*, 359, 207, doi: [10.1038/359207a0](https://doi.org/10.1038/359207a0)
- Christensen-Dalsgaard, J., Duvall, T. L., J., Gough, D. O., Harvey, J. W., & Rhodes, E. J., J. 1985, *Nature*, 315, 378, doi: [10.1038/315378a0](https://doi.org/10.1038/315378a0)
- Christensen-Dalsgaard, J., Gough, D. O., & Thompson, M. J. 1991, *ApJ*, 378, 413, doi: [10.1086/170441](https://doi.org/10.1086/170441)
- Corsaro, E., & De Ridder, J. 2014, *A&A*, 571, A71, doi: [10.1051/0004-6361/201424181](https://doi.org/10.1051/0004-6361/201424181)
- Creevey, O. L., Metcalfe, T. S., Schultheis, M., et al. 2017, *A&A*, 601, A67, doi: [10.1051/0004-6361/201629496](https://doi.org/10.1051/0004-6361/201629496)
- Curtis, J. L., Agüeros, M. A., Douglas, S. T., & Meibom, S. 2019, *ApJ*, 879, 49, doi: [10.3847/1538-4357/ab2393](https://doi.org/10.3847/1538-4357/ab2393)

- Curtis, J. L., Agüeros, M. A., Matt, S. P., et al. 2020, *ApJ*, 904, 140, doi: [10.3847/1538-4357/abbf58](https://doi.org/10.3847/1538-4357/abbf58)
- Cutri, R. M., Skrutskie, M. F., van Dyk, S., et al. 2003, *VizieR Online Data Catalog*, II/246
- Cyburt, R. H., Amthor, A. M., Ferguson, R., et al. 2010, *ApJS*, 189, 240, doi: [10.1088/0067-0049/189/1/240](https://doi.org/10.1088/0067-0049/189/1/240)
- Davies, G. R., Broomhall, A. M., Chaplin, W. J., Elsworth, Y., & Hale, S. J. 2014, *MNRAS*, 439, 2025, doi: [10.1093/mnras/stu080](https://doi.org/10.1093/mnras/stu080)
- de Assis Peralta, R., Samadi, R., & Michel, E. 2018, *Astronomische Nachrichten*, 339, 134, doi: [10.1002/asna.201813469](https://doi.org/10.1002/asna.201813469)
- Delorme, P., Collier Cameron, A., Hebb, L., et al. 2011, *MNRAS*, 413, 2218, doi: [10.1111/j.1365-2966.2011.18299.x](https://doi.org/10.1111/j.1365-2966.2011.18299.x)
- Deming, D., Knutson, H., Kammer, J., et al. 2015, *ApJ*, 805, 132, doi: [10.1088/0004-637X/805/2/132](https://doi.org/10.1088/0004-637X/805/2/132)
- Douglas, S. T., Agüeros, M. A., Covey, K. R., et al. 2016, *ApJ*, 822, 47, doi: [10.3847/0004-637X/822/1/47](https://doi.org/10.3847/0004-637X/822/1/47)
- Dressing, C. D., & Charbonneau, D. 2013, *ApJ*, 767, 95, doi: [10.1088/0004-637X/767/1/95](https://doi.org/10.1088/0004-637X/767/1/95)
- Duquennoy, A., & Mayor, M. 1991, *A&A*, 500, 337
- Duvall, T. L., Jr., Dziembowski, W. A., Goode, P. R., et al. 1984, *Nature*, 310, 22, doi: [10.1038/310022a0](https://doi.org/10.1038/310022a0)
- Engle, S. G., & Guinan, E. F. 2011, in *Astronomical Society of the Pacific Conference Series*, Vol. 451, 9th Pacific Rim Conference on Stellar Astrophysics, ed. S. Qain, K. Leung, L. Zhu, & S. Kwok, 285. <https://arxiv.org/abs/1111.2872>
- Epstein, C. R., & Pinsonneault, M. H. 2014, *ApJ*, 780, 159, doi: [10.1088/0004-637X/780/2/159](https://doi.org/10.1088/0004-637X/780/2/159)
- Esselstein, R., Aigrain, S., Vanderburg, A., et al. 2018, *ApJ*, 859, 167, doi: [10.3847/1538-4357/aac20e](https://doi.org/10.3847/1538-4357/aac20e)
- Ferguson, J. W., Alexander, D. R., Allard, F., et al. 2005, *ApJ*, 623, 585, doi: [10.1086/428642](https://doi.org/10.1086/428642)
- Gaia Collaboration, Brown, A. G. A., Vallenari, A., et al. 2018, *A&A*, 616, A1, doi: [10.1051/0004-6361/201833051](https://doi.org/10.1051/0004-6361/201833051)
- Gilliland, R. L., Brown, T. M., Christensen-Dalsgaard, J., et al. 2010, *PASP*, 122, 131, doi: [10.1086/650399](https://doi.org/10.1086/650399)
- Goulding, N. T., Barnes, J. R., Pinfield, D. J., et al. 2012, *MNRAS*, 427, 3358, doi: [10.1111/j.1365-2966.2012.21932.x](https://doi.org/10.1111/j.1365-2966.2012.21932.x)
- Greco, G., Fossat, E., & Pomerantz, M. A. 1983, *SoPh*, 82, 55, doi: [10.1007/BF00145545](https://doi.org/10.1007/BF00145545)
- Grevesse, N., & Sauval, A. J. 1998, *SSRv*, 85, 161, doi: [10.1023/A:1005161325181](https://doi.org/10.1023/A:1005161325181)
- Gruner, D., & Barnes, S. A. 2020, *A&A*, 644, A16, doi: [10.1051/0004-6361/202038984](https://doi.org/10.1051/0004-6361/202038984)
- Harris, C. R., Millman, K. J., van der Walt, S. J., et al. 2020, *Nature*, 585, 357, doi: [10.1038/s41586-020-2649-2](https://doi.org/10.1038/s41586-020-2649-2)
- Hart, M. H. 1979, *Icarus*, 37, 351, doi: [10.1016/0019-1035\(79\)90141-6](https://doi.org/10.1016/0019-1035(79)90141-6)
- Harvey, J. 1985, in *ESA Special Publication*, Vol. 235, *Future Missions in Solar, Heliospheric & Space Plasma Physics*, ed. E. Rolfe & B. Battrock, 199
- Hawley, S. L., & Pettersen, B. R. 1991, *ApJ*, 378, 725, doi: [10.1086/170474](https://doi.org/10.1086/170474)
- Hey, D., & Ball, W. 2020, *Echelle: Dynamic echelle diagrams for asteroseismology*, 1.4, Zenodo, doi: [10.5281/zenodo.3629933](https://doi.org/10.5281/zenodo.3629933)
- Høg, E., Fabricius, C., Makarov, V. V., et al. 2000, *A&A*, 355, L27
- Howell, S. B., Sobeck, C., Haas, M., et al. 2014, *PASP*, 126, 398, doi: [10.1086/676406](https://doi.org/10.1086/676406)
- Huber, D., Chaplin, W. J., Christensen-Dalsgaard, J., et al. 2013, *ApJ*, 767, 127, doi: [10.1088/0004-637X/767/2/127](https://doi.org/10.1088/0004-637X/767/2/127)
- Huber, D., Bryson, S. T., Haas, M. R., et al. 2016, *ApJS*, 224, 2, doi: [10.3847/0067-0049/224/1/2](https://doi.org/10.3847/0067-0049/224/1/2)
- Hunter, J. D. 2007, *Computing in Science & Engineering*, 9, 90, doi: [10.1109/MCSE.2007.55](https://doi.org/10.1109/MCSE.2007.55)
- Iglesias, C. A., & Rogers, F. J. 1996, *ApJ*, 464, 943, doi: [10.1086/177381](https://doi.org/10.1086/177381)

- J.A. Nelder, & R. Mead. 1965, *The Computer Journal*, 7, 308
- Kasting, J. F., Whitmire, D. P., & Reynolds, R. T. 1993, *Icarus*, 101, 108, doi: [10.1006/icar.1993.1010](https://doi.org/10.1006/icar.1993.1010)
- Kawaler, S. D. 1988, *ApJ*, 333, 236, doi: [10.1086/166740](https://doi.org/10.1086/166740)
- Kjeldsen, H., Bedding, T. R., & Christensen-Dalsgaard, J. 2008, *ApJL*, 683, L175, doi: [10.1086/591667](https://doi.org/10.1086/591667)
- Kraft, R. P. 1967, *ApJ*, 150, 551, doi: [10.1086/149359](https://doi.org/10.1086/149359)
- Krishna Swamy, K. S. 1966, *ApJ*, 145, 174, doi: [10.1086/148752](https://doi.org/10.1086/148752)
- Lammer, H., Lichtenegger, H. I. M., Kulikov, Y. N., et al. 2007, *Astrobiology*, 7, 185, doi: [10.1089/ast.2006.0128](https://doi.org/10.1089/ast.2006.0128)
- Lammer, H., Bredehöft, J. H., Coustenis, A., et al. 2009, *A&A Rv*, 17, 181, doi: [10.1007/s00159-009-0019-z](https://doi.org/10.1007/s00159-009-0019-z)
- Lammer, H., Blanc, M., Benz, W., et al. 2013, *Astrobiology*, 13, 793, doi: [10.1089/ast.2013.0997](https://doi.org/10.1089/ast.2013.0997)
- Lanzafame, A. C., & Spada, F. 2015, *A&A*, 584, A30, doi: [10.1051/0004-6361/201526770](https://doi.org/10.1051/0004-6361/201526770)
- Libbrecht, K. 1989, *S&T*, 77, 584
- Lightkurve Collaboration, Cardoso, J. V. d. M., Hedges, C., et al. 2018, *Lightkurve: Kepler and TESS time series analysis in Python*, *Astrophysics Source Code Library*. <http://ascl.net/1812.013>
- Lomb, N. R. 1976, *Ap&SS*, 39, 447, doi: [10.1007/BF00648343](https://doi.org/10.1007/BF00648343)
- Lu, Y. L., Angus, R., Curtis, J. L., David, T. J., & Kiman, R. 2021, *AJ*, 161, 189, doi: [10.3847/1538-3881/abe4d6](https://doi.org/10.3847/1538-3881/abe4d6)
- Luger, R., Agol, E., Kruse, E., et al. 2016, *AJ*, 152, 100, doi: [10.3847/0004-6256/152/4/100](https://doi.org/10.3847/0004-6256/152/4/100)
- Luger, R., & Barnes, R. 2015, *Astrobiology*, 15, 119, doi: [10.1089/ast.2014.1231](https://doi.org/10.1089/ast.2014.1231)
- Luger, R., Kruse, E., Foreman-Mackey, D., Agol, E., & Saunders, N. 2018, *AJ*, 156, 99, doi: [10.3847/1538-3881/aad230](https://doi.org/10.3847/1538-3881/aad230)
- MacGregor, K. B., & Brenner, M. 1991, *ApJ*, 376, 204, doi: [10.1086/170269](https://doi.org/10.1086/170269)
- Mamajek, E. E., & Hillenbrand, L. A. 2008, *ApJ*, 687, 1264, doi: [10.1086/591785](https://doi.org/10.1086/591785)
- Mann, A. W., Feiden, G. A., Gaidos, E., Boyajian, T., & von Braun, K. 2015, *ApJ*, 804, 64, doi: [10.1088/0004-637X/804/1/64](https://doi.org/10.1088/0004-637X/804/1/64)
- McQuillan, A., Mazeh, T., & Aigrain, S. 2014, *ApJS*, 211, 24, doi: [10.1088/0067-0049/211/2/24](https://doi.org/10.1088/0067-0049/211/2/24)
- Meibom, S., Barnes, S. A., Platais, I., et al. 2015, *Nature*, 517, 589, doi: [10.1038/nature14118](https://doi.org/10.1038/nature14118)
- Meibom, S., Mathieu, R. D., & Stassun, K. G. 2009, *ApJ*, 695, 679, doi: [10.1088/0004-637X/695/1/679](https://doi.org/10.1088/0004-637X/695/1/679)
- Meibom, S., Barnes, S. A., Latham, D. W., et al. 2011, *ApJL*, 733, L9, doi: [10.1088/2041-8205/733/1/L9](https://doi.org/10.1088/2041-8205/733/1/L9)
- Metcalfe, T., Creevey, O., & van Saders, J. 2017, in *European Physical Journal Web of Conferences*, Vol. 152, *European Physical Journal Web of Conferences*, 05001, doi: [10.1051/epjconf/201715205001](https://doi.org/10.1051/epjconf/201715205001)
- Montes, D., González-Peinado, R., Taberner, H. M., et al. 2018, *MNRAS*, 479, 1332, doi: [10.1093/mnras/sty1295](https://doi.org/10.1093/mnras/sty1295)
- Nutzman, P., & Charbonneau, D. 2008, *PASP*, 120, 317, doi: [10.1086/533420](https://doi.org/10.1086/533420)
- Parker, E. N. 1958, *ApJ*, 128, 664, doi: [10.1086/146579](https://doi.org/10.1086/146579)
- Paxton, B., Bildsten, L., Dotter, A., et al. 2011, *ApJS*, 192, 3, doi: [10.1088/0067-0049/192/1/3](https://doi.org/10.1088/0067-0049/192/1/3)
- Paxton, B., Cantiello, M., Arras, P., et al. 2013, *ApJS*, 208, 4, doi: [10.1088/0067-0049/208/1/4](https://doi.org/10.1088/0067-0049/208/1/4)
- Paxton, B., Marchant, P., Schwab, J., et al. 2015, *ApJS*, 220, 15, doi: [10.1088/0067-0049/220/1/15](https://doi.org/10.1088/0067-0049/220/1/15)
- Paxton, B., Schwab, J., Bauer, E. B., et al. 2018, *ApJS*, 234, 34, doi: [10.3847/1538-4365/aaa5a8](https://doi.org/10.3847/1538-4365/aaa5a8)
- Paxton, B., Smolec, R., Schwab, J., et al. 2019, *ApJS*, 243, 10, doi: [10.3847/1538-4365/ab2241](https://doi.org/10.3847/1538-4365/ab2241)

- Pinsonneault, M. H., Kawaler, S. D., & Demarque, P. 1990, *ApJS*, 74, 501, doi: [10.1086/191507](https://doi.org/10.1086/191507)
- Pols, O. R. 2011, *Stellar Structure and Evolution*, Tech. rep.
- Rebull, L. M., Stauffer, J. R., Hillenbrand, L. A., et al. 2017, *ApJ*, 839, 92, doi: [10.3847/1538-4357/aa6aa4](https://doi.org/10.3847/1538-4357/aa6aa4)
- Rebull, L. M., Stauffer, J. R., Bouvier, J., et al. 2016, *AJ*, 152, 113, doi: [10.3847/0004-6256/152/5/113](https://doi.org/10.3847/0004-6256/152/5/113)
- Rodríguez, E., Rodríguez-López, C., López-González, M. J., et al. 2016, *MNRAS*, 457, 1851, doi: [10.1093/mnras/stw033](https://doi.org/10.1093/mnras/stw033)
- Scargle, J. D. 1982, *ApJ*, 263, 835, doi: [10.1086/160554](https://doi.org/10.1086/160554)
- Seaton, M. J., Yan, Y., Mihalas, D., & Pradhan, A. K. 1994, *MNRAS*, 266, 805, doi: [10.1093/mnras/266.4.805](https://doi.org/10.1093/mnras/266.4.805)
- Shields, A. L., Ballard, S., & Johnson, J. A. 2016, *PhR*, 663, 1, doi: [10.1016/j.physrep.2016.10.003](https://doi.org/10.1016/j.physrep.2016.10.003)
- Silva Aguirre, V., Lund, M. N., Antia, H. M., et al. 2017, *ApJ*, 835, 173, doi: [10.3847/1538-4357/835/2/173](https://doi.org/10.3847/1538-4357/835/2/173)
- Skumanich, A. 1972, *ApJ*, 171, 565, doi: [10.1086/151310](https://doi.org/10.1086/151310)
- Soderblom, D. R. 1983, *ApJS*, 53, 1, doi: [10.1086/190880](https://doi.org/10.1086/190880)
- . 2010, *ARA&A*, 48, 581, doi: [10.1146/annurev-astro-081309-130806](https://doi.org/10.1146/annurev-astro-081309-130806)
- Somers, G., & Pinsonneault, M. H. 2016, *ApJ*, 829, 32, doi: [10.3847/0004-637X/829/1/32](https://doi.org/10.3847/0004-637X/829/1/32)
- Spada, F., & Lanzafame, A. C. 2020, *A&A*, 636, A76, doi: [10.1051/0004-6361/201936384](https://doi.org/10.1051/0004-6361/201936384)
- Tayar, J., Claytor, Z. R., Huber, D., & van Saders, J. 2020, arXiv e-prints, arXiv:2012.07957. <https://arxiv.org/abs/2012.07957>
- The Pandas Development Team. 2020, pandas-dev/pandas: Pandas, latest, Zenodo, doi: [10.5281/zenodo.3509134](https://doi.org/10.5281/zenodo.3509134)
- Thoul, A. A., Bahcall, J. N., & Loeb, A. 1994, *ApJ*, 421, 828, doi: [10.1086/173695](https://doi.org/10.1086/173695)
- Tokovinin, A. 2014, *AJ*, 147, 86, doi: [10.1088/0004-6256/147/4/86](https://doi.org/10.1088/0004-6256/147/4/86)
- Torres, G., Fischer, D. A., Sozzetti, A., et al. 2012, *ApJ*, 757, 161, doi: [10.1088/0004-637X/757/2/161](https://doi.org/10.1088/0004-637X/757/2/161)
- Townsend, R. H. D., & Teitler, S. A. 2013, *MNRAS*, 435, 3406, doi: [10.1093/mnras/stt1533](https://doi.org/10.1093/mnras/stt1533)
- Vanderburg, A., & Johnson, J. A. 2014, *PASP*, 126, 948, doi: [10.1086/678764](https://doi.org/10.1086/678764)
- Virtanen, P., Gommers, R., Oliphant, T. E., et al. 2020, *Nature Methods*, 17, 261, doi: [10.1038/s41592-019-0686-2](https://doi.org/10.1038/s41592-019-0686-2)
- Vorontsov, S. V. 1989, *Soviet Astronomy Letters*, 15, 21
- Weber, E. J., & Davis, Leverett, J. 1967, *ApJ*, 148, 217, doi: [10.1086/149138](https://doi.org/10.1086/149138)
- Wes McKinney. 2010, in *Proceedings of the 9th Python in Science Conference*, ed. Stéfan van der Walt & Jarrod Millman, 56 – 61, doi: [10.25080/Majora-92bf1922-00a](https://doi.org/10.25080/Majora-92bf1922-00a)
- Whitworth, A. P., Chapman, S. J., Bhattal, A. S., et al. 1995, *MNRAS*, 277, 727, doi: [10.1093/mnras/277.2.727](https://doi.org/10.1093/mnras/277.2.727)
- Yu, J., Huber, D., Bedding, T. R., et al. 2018, *ApJS*, 236, 42, doi: [10.3847/1538-4365/aaaf74](https://doi.org/10.3847/1538-4365/aaaf74)